ESA Cloud_cci

Algorithm Theoretical Baseline Document v9.0
Community Cloud retrieval for Climate (CC4CL)

Issue 9 Revision 0

3/5/2023

Deliverable No.: D-2.1
ESRIN/Contract No.: 4000128637/20/I-NB
Project Coordinator: Dr. Martin Stengel
Deutscher Wetterdienst
martin.stengel@dwd.de
Technical Officer: Michael Eisinger
European Space Agency
Michael.Eisinger@esa.int
Document authors: Gareth E. Thomas[1], Caroline A. Poulsen[4], Richard Siddans[1], Adam Povey[2]
Andrew T. Prata[2+], Daniel Philipp[3], Martin Stengel[3], Simon Proud[1,2]
Greg McGarragh[2+], Cornelia Schlundt[3+], Stefan Stapelberg[3+]
Roy G. Grainger[2]

[1] RAL Space, STFC-RAL, Harwell Campus, Didcot, OX11 0QX, UK
[2] Atmospheric, Oceanic and Planetary Physics, University of Oxford, Oxford, OX1 3PU, UK
[3] Deutscher Wetterdienst, Frankfurter Str. 135, 63067 Offenbach, Germany
[4] Bureau of Meteorology, 700 Collins St, Docklands, Melbourne VIC 3001, Australia
[+] Author affiliation outdated, but correct at time of contribution

Contents

Document Change Record

Document, Version	Date	Changes	Originator
ATBD Version 5.1	12/09/2017	Released precursor version of ATBD applicable for Cloudcci dataset version 2	Caroline A. Poulsen, Gareth E. Thomas, Richard Siddans, Adam Povey, Greg McGarragh, Cornelia Schlundt, Stefan Stapelberg, Martin Stengel, Roy G. Grainger
ATBD Version 6.0	27/09/2018	Revision to make this document representing CC4CL used for processing of AVHRR-AM/PMv3 and ATSR2-AATSRv3 datasets. e.g. - renaming subsection on night retrievals to new subsection 2.4.9 including cloud emissivity retrieval Version submitted to ESA for review.	Caroline A. Poulsen, Gareth E. Thomas, Richard Siddans, Adam Povey, Greg McGarragh, Cornelia Schlundt, Stefan Stapelberg, Martin Stengel, Roy G. Grainger
ATBD Version 6.1	29/01/2019	Updates after ESA review of document version 6.0. E.g. - updating introduction section - updating section 2.1 on cloud detection ANN - updating section 2.2 on cloud phase ANN - introducing new subsection on spectral band adjustment - minor updates of subsection 2.4. - introducing new subsection 2.4.16 - modifying subsection 2.5 - introducing new subsection 2.6 on changes from previous to current CC4CL version.	Caroline A. Poulsen, Martin Stengel
ATBD Version 6.2	11/03/2019	Updates after ESA review of document version 6.1. E.g. - Introducing new subsection 2.4.17 on new Aerosol-Cloud (and sunglint) discrimination tests - Addiing bullet point in Section 2.6 mentioning the usage of USGS 0.5km MODIS based Land Cover Type 2 data - Editing some text in Section 3 including mentioning options on using different snow/ice masks and on using higher resolved land/sea masks	Martin Stengel

Document, Version	Date	Changes	Originator
ATBD Version 7.0	15/03/2021	- Updated to reflect the move from ERA-Interim to ERA5. - Included SLSTR and SEVIRI input data description. - Described new SEVIRI cloud detection and phase determination networks in appendix D - Added introduction of new SEVIRI networks to section 2 - Added Sentinel-3A/3B SLSTR and MSG1/2/3/4 SEVIRI SBA coefficients to table 5 and 6 + moved SBA section to appendix A - Added appendix C on using the spectral response functions for the LUTs.	Gareth Thomas, Martin Stengel, Daniel Philipp, Roy Grainger, Simon Proud
ATBD Version 8.0	09/03/2022	- Added information how SEVIRI visible channel inconsistencies between CC4CL and external ANNs were solved in appendix D (new: table 7). - Added appendix C on using the spectral response functions for the LUTs. - Added sec. 2.3.12 on CDNC products and 2.3.13 on cloud thickness. -Added section 2.3.16 on the use of 1.38 μm reflectance for cloud detection and height estimation. -Added information in section2.3.1 on ice model sensitivity studies done including a link to the supplementary document that holds the results.	Gareth Thomas, Martin Stengel, Daniel Philipp, Roy Grainger, Adam Povey, Simon Proud
ATBD Version 9.0	28/02/2023	- Updated SEVIRI CMA/CPH ANNs in appendix D reflecting changes implemented for v3 data. - Updated section2 to latest SEVIRI_ML developments as the CMA and CPH ANNs have been integrated in to a formalized software library called SEVIRI_ML and updated to v3.	Gareth Thomas, Martin Stengel, Daniel Philipp, Roy Grainger, Adam Povey, Simon Proud

1 Introduction

This document describes an optimal estimation retrieval scheme for the derivation of the properties of clouds from top-of-atmosphere (TOA) radiances measured by satellite-borne visible-IR radiometers as described in detail by McGarragh et al. [22], Sus el al. [40], Poulsen et al. [28] and Watts et al. [45]. The algorithm makes up part of the Community Code for CLimate (CC4CL) retrieval scheme (the other part, known as ORAC or the Optimal Retrieval of Aerosol and Cloud, performs aerosol retrievals and is described in Thomas et al. [43]). CC4CL was originally designed for application to SEVIRI and was subsequently adapted for the ATSR instrument, which was used to produce the GRAPE (Global Retrieval of ATSR cloud Parameters and Evaluation) data set. During previous phases the Cloud_cci framework, the algorithm has been applied to AVHRR and MODIS using the 'heritage' set of channels (i.e. channels equivalent to the 0.67, 0.87, 1.6, 3.7, 11 and 12 μm channels of AVHRR) to produce a long-term climate data record with global coverage. The algorithm has also been adapted to retrieve cloud properties from the VIIRS, AHI, AGRI, GOES, Himawari and SEVIRI instruments.

The focus of the current phase of Cloud_cci is the further development of CC4CL to exploit the Sea and Land Surface Temperature (SLSTR) and Spinning Enhanced Visible and InfraRed Imager (SEVIRI) instruments, going beyond the heritage channels to make full use of the capabilities of these instruments. The algorithm can ingest most visible and Infrared wavelengths and considerable performance enhancement can be achieved when additional channels are used in the retrieval. For example improved cloud top height is achieved when the CO_2 slicing channels are used. In the text that follows, the description will often refer to AATSR but is equally applicable to instruments with similar channel definitions.

Specific features of this algorithm include:

- A full implementation of the optimal estimation framework described by Rodgers [31], enabling rigorous error propagation and inclusion of *a priori* knowledge.
- A common retrieval algorithm over both land and ocean, with only the *a priori* constraint on the surface reflectance differing between the two.
- Consistent and simultaneous retrieval of all cloud parameters in the visible and infrared.

2 Retrieval system description

CC4CL consists of three main components: (1) cloud detection (2) cloud typing and (3) the retrieval of cloud properties based on OE technique. These components are described in more detail in the following sections.

With the current phase of Cloud_cci and its focus on going beyond the AVHRR-heritage channels a novel SEVIRI cloud masking and cloud phase determination algorithm was introduced (`https://github.com/danielphilipp/seviri_ml`) using SEVIRI's full spectral capabilities. Basically both algorithms share the same technique of applying Artificial Neural Networks (ANNs) trained to predict CALIPSO cloud optical depth (for cloud masking) or CALIPSO cloud phase (for phase determination) followed by subsequent thresholding and uncertainty estimation. Together with the cloud masking / cloud phase determination algorithms developed in previous phases of Cloud_cci there are now two possibilities:

1. The AVHRR-heritage channel based cloud mask / cloud phase ANN developed in the previous Cloud_cci phase which allows for a consistent processing throughout all sensors. It is part of the CC4CL core code. See below section 2.1 and section 2.2 for a detailed description.
2. An external SEVIRI Artificial Neural network (ANN) cloud masking and cloud phase determination algorithm within the SEVIRI_ML software suite (`https://github.com/danielphilipp/seviri_`

ml) using almost SEVIRI's full spectral capabilities with better performance than the AVHRR heritage ANNs. SEVIRI_ML can be integrated into CC4CL using a Python-Fortran-C interface. Since version 3, the SEVIRI-specific cloud detection and cloud phase determination ANNs are included within SEVIRI_ML which also contains ANNs for more cloud-related parameters. Version 2 and version 1 cloud mask and cloud phase ANNs can also be called with SEVIRI_ML. See appendix D.1 for more information.

The SEVIRI_ML ANNs are applied to SEVIRI and the heritage ANNs to SLSTR. However, to obtain the best performance from the heritage ANN it is recommended to apply the Spectral Band Adjustment (SBA) coefficients (see section A) to the instrument's measurements. Lately SLSTR and SEVIRI SBA coefficients have been added to the code as well as table 5 and table 6.

2.1 AVHRR-heritage cloud detection

The cloud mask is based on artificial neural networks (ANNs). Three ANNs were trained: for day (using visible (VIS), near-infrared (NIR) and infrared (IR) information), for night/twilight (using NIR and IR channels), and again for night/twilight with different channel input (IR channels only). The ANNs have been trained based on collocations between AVHRR NOAA-19 measurements and CALIPSO COD data. As a result a pseudo CALIPSO optical depth (ANNCOD) is computed (mimicked) and converted into a 2 bit cloud mask by applying thresholds.

The used ANN's are multilayer perceptrons consisting of 1 input layer, one hidden layer with about 50 neurons and one output layer. The training and test data sets are based on collocated CALIPSO COD data (CAL_LID_L2_05kmCLay-Prov-V3-01, total optical thickness at 532nm) and Cloud_cci AVHRR GAC Level-1C measurements. The Day ANN was trained with VIS and IR data. Compared to earlier versions, Ch3b (3.7 µm) of AVHRR was now included Day ANN. For NOAA-17, METOP-A and partly NOAA-16 a separate ANN was trained including $1.6\mu m$ instead of $3.7\mu m$ during day. The 2 night ANN's have been trained both with and without the $3.7\mu m$ NIR channel information. This avoids the misclassification of very cold clouds and/or surfaces because of very low $3.7\mu m$ channel signal–to-noise-ratios. The channel input is again summarizes in table 1.

Overall, 5 years of globally and seasonally representative collocation data between NOAA-19 and CALIPSO have been chosen as training dataset. Prior to that, all collocated CALIPSO COD's greater 1 have been set to 1. In a final step, a simple viewing-angle correction is applied to the retrieved ANNCOD which tends to increase with increasing viewing-angle. For the generation of the final 2-bit cloud mask, suitable thresholds have been found and applied to the ANNCOD.

Cloud detection thresholds:
Table 2 lists the threshold applied to determine the binary cloud decision from ANNCOD. The thresholds depend on illumination and surface type.

As the ANNs were trained using NOAA-19 AVHRR measurements, a radiances adjustment has been determined for AATSR, MODIS, SLSTR and SEVIRI to make them mimic AVHRR. The adjustment includes slopes and offsets based on synthetic measurements with details given in Section A.

Cloud detection uncertainty:
Based on the training set. The binary results (after applying ANN and thresholds) were compared against the CALIOP cloud mask and detection scores calculated. The scores show a clear dependence on the distance between the ANNCOD and the respective threshold, which allows a approximation of the cloud detection uncertainty on pixel level based on these two values. Figure 1 shows the probability of incorrect cloud mask as a function of normalized ANNCOD-threshold distance.

Table 1: Measurement input to the trained artificial neural network for cloud detection (ANN_{mask}), used for different illumination conditions: daytime, twilight and night-time. The subscript in the table's headline corresponds to the approximate central wavelengths of the channels: 0.6µm, 0.9µm, 1.6µm, 3.7µm, 10.8µm, 12.0µm. In addition to the measurement input, all ANNs require surface temperature, a snow-ice flag and a land-sea flag as input. R=reflectance, BT=brightness temperature

ANN_{mask}	$R_{0.6}$	$R_{0.9}$	$R_{1.6}$	$R_{3.7}$	$BT_{3.7}$	$BT_{10.8}$	$BT_{12.0}$	$BT_{10.8}$-$BT_{12.0}$	$BT_{10.8}$-$BT_{3.7}$
$Day_{3.7}$	✓	✓	-	✓	-	✓	✓	✓	-
$Day_{1.6}$	✓	✓	✓	-	-	✓	✓	✓	-
Day_{backup}	✓	✓	-	-	-	✓	✓	✓	-
$Twilight_{3.7}$	-	-	-	-	✓	✓	✓	✓	✓
$Twilight_{backup}$	-	-	-	-	-	✓	✓	✓	-
$Night_{3.7}$	-	-	-	-	✓	✓	✓	✓	✓
$Night_{backup}$	-	-	-	-	-	✓	✓	✓	-

Table 2: Thresholds used to convert the output of the cloud mask ANNs to a binary cloud mask. Thresholds depend on illumination conditions and surface types.

Illumination	Surface type	Threshold
Day	Sea ice	0.4
Day	Land ice	0.3
Day	Sea	0.25
Day	Land	0.3
Night	Sea ice	0.45
Night	Land ice	0.35
Night	Sea	0.25
Night	Land	0.3
Twilight	Sea ice	0.5
Twilight	Land ice	0.35
Twilight	Sea	0.35
Twilight	Land	0.45

2.2 AVHRR-heritage cloud type and phase determination

A new cloud typing algorithm has been implemented in the preprocessing to select a cloud phase based on the cloud type it selects:

Cloud type:

- The following categories indicate the liquid cloud phase:
  - fog,
  - warm liquid water clouds, and
  - supercooled-mixed-phased clouds.
- The following categories indicate the ice cloud phase:
  - opaque ice clouds/deep convection,

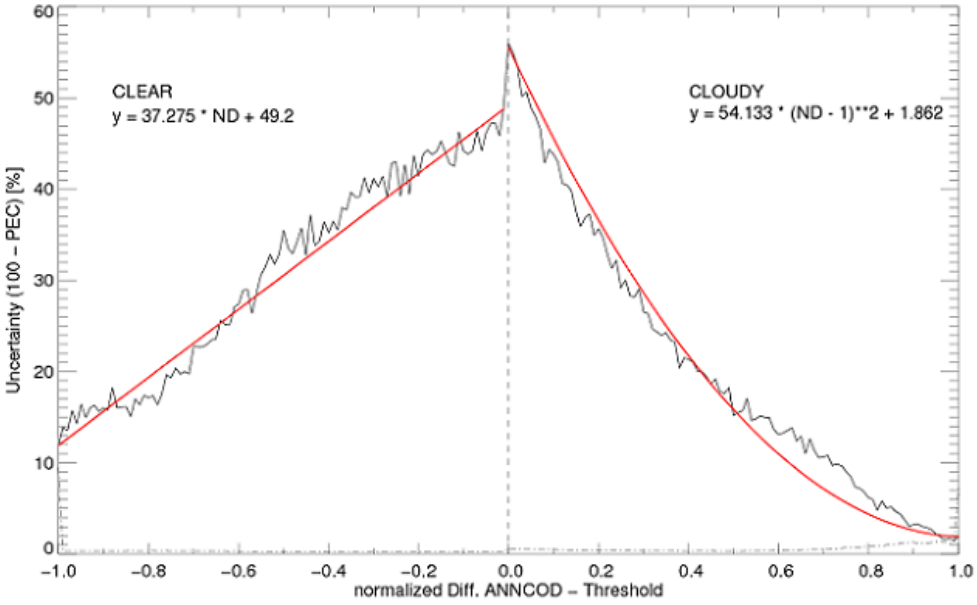

Figure 1: AVHRR-heritage neural network cloud mask uncertainty. Figure taken from Sus el al. [40]

- non-opaque high ice clouds (e.g. cirrus),
- cloud overlap[1] (e.g. multiple cloud layers), and
- probably-opaque ice clouds (e.g. neither 1.6 μm nor 3.7 μm channel is available during night for AVHRR; 12 μm channel is missing during night for AATSR).

Usually, CC4CL performs separate retrievals for each phase and selects the appropriate phase as that with the lowest retrieval cost (eqn. 1). If desired, CC4CL can now process only once assuming the phase identified above.

A detailed description of daytime spectral tests using AVHRR, MODIS and VIIRS observations is given in Pavolonis and Heidinger [26] and Pavolonis et al. [27] along with inter-comparison results. The multispectral algorithm used in CC4CL is based on the threshold approach described in these papers but can retrieve in the absence of visible/near-IR measurements (e.g. at night) and includes a new threshold test required for AVHRR and A(A)TSR measurements (i.e. the probably-opaque ice clouds).

To briefly summarize the main features of the algorithm, the cloud type retrieval requires as input satellite imager data at 0.65, 1.6(3a)/3.75(3b), 10.8 and 12 μm. If both 1.6 and 3.75 μm data are available, the 3.75 μm reflectances are used.[2] Pavolonis et al. [27] have analyzed cloud typing results based on channel 3a or 3b and concluded that both algorithms produce nearly identical results except for certain thin clouds and at cloud edges. More often than the 3b algorithm, the retrieval using 3a tends to misclassify the thin edges of some low and mid-level clouds as cirrus and opaque ice.

The algorithm also requires a cloud mask as only satellite pixels which are fully covered by cloud should be processed. Pavolonis et al. [27] have shown that if any clear pixels are passed to the cloud typing code, they would mostly be identified as warm liquid water or supercooled-mixed-phase cloud depending on the

[1] Assuming that a scene with cloud overlap consists of a semitransparent ice cloud that overlaps a cloud composed of liquid water droplets [26].

[2] AVHRR sensors mounted on NOAA-7, 9, 11, 12 and 14 have only five channels (3a is missing). NOAA-15 through NOAA-19 as well as MetOp-A and MetOp-B have six channels, but only 5 channels are transmitted simultaneously, such that there is a potential switch in availability between 3a and 3b for certain time periods and sensors (generally 3a during the day and 3b during the night).

brightness temperature at 11 μm over most surface types and as opaque ice cloud over cold snow/ice covered surfaces.

Finally, the surface type of each single satellite pixel is required because different threshold values are applied depending on the underlying surface, particularly for water, desert and snow/ice.

Cloud phase:
While in the previous CC4CL version, the cloud types were just converted to a binary cloud phase, in the present CC4CL version an ANN for cloud phase was developed and implemented.

Three ANNs were trained: for day (using visible (VIS), near-infrared (NIR) and infrared (IR) information), for night/twilight (using NIR and IR channels), and again for night/twilight with different channel input (IR channels only). The ANNs have been trained based on collocations between AVHRR NOAA-19 measurements and CALIPSO CPH (cloud phase) data. The output of the phase ANN is a pseudo CALIPSO cloud phase although giving continuous values between 0 (liquid) and 1 (ice) which requires the application of thresholds posterior to infer 2 bit cloud phase information mask by applying thresholds.

As for cloud detection, the used ANN's are multilayer perceptrons consisting of 1 input layer, one hidden layer with about 50 neurons and one output layer. The training and test data sets are based on 5 years of collocated CALIPSO CPH data (CAL_LID_L2_05kmCLay-Prov-V3-01) and NOAA-19 AVHRR GAC Level-1C measurements. The Day ANN was trained with VIS, NIR and IR data. As defaults the 3.7 µm channel is expected; for NOAA-17, METOP-A and partly NOAA-16 a separate ANN was trained including 1.6μm instead of 3.7μm during day. The 2 night ANN's have been trained both with and without the 3.7μm NIR channel information. The channel input is again summarizes in table 3. A simple viewing-angle correction is applied to the ANN output. For the generation of the final 2-bit cloud phase, suitable thresholds have been found and applied.

Cloud phase thresholds:
Table 4 lists the threshold applied to determine the binary cloud phase from ANN output. The thresholds depend on illumination and surface type.

As the ANNs were trained using NOAA-19 AVHRR measurements, a radiances adjustment has been determined for AATSR, MODIS, SLSTR and SEVIRI to make them mimic AVHRR. The adjustment includes slopes and offsets based on synthetic measurements with details given in Section A.

Cloud phase uncertainty:
Cloud phase uncertainty is done in an identical fashion as for cloud detection (see above).

Table 3: Measurement input to the trained artificial neural network for cloud phase determination (ANN_{phase}, used for different illumination conditions: daytime, twilight and night-time. The subscript in the table's headline corresponds to the approximate central wavelengths of the channels: 0.6µm, 0.9µm, 1.6µm, 3.7µm, 10.8µm, 12.0µm. In addition to the measurement input, all ANNs require a surface type flag containing the values 0:sea,1:land,2:desert,3:sea-ice,4:snow.

ANN_{phase}	$R_{0.6}$	$R_{0.9}$	$R_{1.6}$	$R_{3.7}$	$BT_{3.7}$	$BT_{10.8}$	$BT_{12.0}$	$BT_{10.8}$-BT12.0	$BT_{10.8}$-BT3.7
$Day_{3.7}$	✓	✓	-	✓	-	✓	✓	✓	-
$Day_{1.6}$	✓	✓	✓	-	-	✓	✓	✓	-
Twilight	-	-	-	-	✓	✓	✓	✓	✓
Night	-	-	-	-	✓	✓	✓	✓	✓

Table 4: Thresholds used to convert the output of the cloud phase ANNs to a binary cloud phase. Thresholds depend on illumination conditions and surface types.

Illumination	Surface type	Threshold
Day	Sea ice	0.5
Day	Land ice	0.7
Day	Sea	0.55
Day	Land	0.7
Night	Sea ice	0.7
Night	Land ice	0.6
Night	Sea	0.5
Night	Land	0.65
Twilight	Sea ice	0.7
Twilight	Land ice	0.9
Twilight	Sea	0.65
Twilight	Land	0.50

2.3 Cloud property retrieval algorithm

Although the algorithm described here is applicable to measurements in a wide range of visible to thermal infrared atmospheric window channels, within the Cloud_cci project it is being applied to the so-called *heritage channels* first used on the AVHRR series of instruments. These are six channels centred around 0.67, 0.87, 1.6, 3.7, 11, and 12 μm (although there can be considerable differences in the widths and central wavelengths of filter band-passes in different instruments). These channels are sensitive in different ways to the macro and microphysical properties of cloud. For example, the infrared channels compliment the visible channels in the case of optically thin clouds. However, the observations are not sensitive to every aspect of the three-dimensional distribution of all relevant cloud properties and no single channel is uniquely sensitive to a specific cloud property.

We approach the problem of extracting useful information on cloud as an inverse problem. A forward model (FM) is defined which applies a radiative transfer model (RTM) to simulate satellite radiances based on a parameterized cloud / atmosphere / surface model (CM) and the prescribed observing conditions. An inverse or retrieval model (RM) is then used to obtain the cloud parameters which give the best fit between the model predicted and observed radiances, taking into account measurement uncertainties and relevant prior knowledge. This inverse problem is solved using the optimal estimation method [31] (OEM).

The basic principle of the OEM is to maximise the probability of the retrieved state, conditional on the value of the measurements and any *a priori* knowledge. Formally, it maximises the conditional probability $P = P(\vec{x}|\vec{y},\ \vec{x_{\rm a}})$ with respect to the values of the measurement vector $\vec{y}$, state vector $\vec{x}$, and *a priori* estimate of the state $\vec{x}_{\rm a}$ (i.e. the most likely state prior to considering the measurements). It is assumed that errors in the measurements, forward model and *a priori* parameters are normally distributed with zero mean and covariances given by $\mathbf{S}_y$ and $\mathbf{S}_{\rm a}$, respectively. The solution state is found by minimising the cost function J:

$$J(\vec{x}) = [\vec{y}(\vec{x}) - \vec{y_{\rm m}}]\,\mathbf{S_y}^{-1}\,[\vec{y}(\vec{x}) - \vec{y_{\rm m}}]^T + (\vec{x} - \vec{x_{\rm a}})\,\mathbf{S}_{\rm a}{}^{-1}\,(\vec{x} - \vec{x_{\rm a}})^T\,. \quad (1)$$

Starting from some initial guess of the state and linearising the forward model, the gradient of the cost function is estimated. Using that, a state is selected which is predicted to have lower cost. The Levenberg-Marquart [21, 18] scheme is used to perform the minimisation. The procedure is iterated until the change in cost between iterations is less than $0.05m$, where m is the length of $\vec{y}$, (called convergence) or the retrieval is abandoned after 40 iterations.

If the *a priori* and measurement uncertainties are well represented by their respective covariances, the value of the cost function at solution is expected to be sampled from a χ^2 distribution with degrees of freedom (approximately) equal to the total number of elements in the measurement and state vectors. Hence, J at convergence provides a measure of the likelihood of the solution-state being consistent with observations and prior knowledge.

For retrievals which satisfactorily converge, i.e. converge to a minimum cost which is consistent with measurement and prior uncertainties, the uncertainty on the estimated state parameters is described by the solution covariance

$$\mathbf{S}_{\mathrm{x}} = (\mathbf{K}^T \mathbf{S}_{\mathrm{y}}^{-1} \mathbf{K} + \mathbf{S}_{\mathrm{a}}^{-1})^{-1}, \tag{2}$$

where $\mathbf{K}$ contains the derivatives of the forward model with respect to each solution state parameter:

$$K_{i,j} = \frac{\partial y_i}{\partial x_j}. \tag{3}$$

2.3.1 Cloud / Atmosphere / Surface Model

The retrieval forward model can be considered to consist of three components: a scattering cloud layer is located within a clear-sky atmosphere over a surface of known reflectance/emissivity. The clear-sky atmosphere is defined by temperature and humidity profiles taken from ECMWF ERA5 analyses [15]. For window channels, the influence of variations in trace gas concentrations, as well as the uncertainties in ECMWF water vapour profiles, are well within the measurement noise. However, if sounding channels (such as the water-vapour channels of SEVIRI) are used, errors in the reanalysis fields could be significant and should be investigated on a case-by-case basis.

The surface is characterised by a bidirectional reflectance distribution function (BRDF) which is computed differently for ocean and land surface. The BRDF over ocean is computed using the methodology outlined by [34] which includes 3 components:

$$\rho(\theta_0, \theta_v, \phi, \lambda, u, v) = \rho_{\mathrm{sg}}(\theta_0, \theta_v, \phi, \lambda, u, v) + \rho_{\mathrm{wc}}(\lambda, u, v) + \rho_{\mathrm{ul}}(\theta_0, \theta_v, \lambda, C), \tag{4}$$

where ρ_{sg} is the sun-glint off wave facets [6], ρ_{wc} is the reflectance from surface foam, so-called "whitecaps" [16], and ρ_{ul} is the scattering from the within the water, so-called "underlight" [24]. In addition, physical parameters include the horizontal wind vector u and v (m/s) and the ocean pigment concentration C (mg/m^3).

The BRDF over land is a weighted sum of an isotropic kernel (unity) and two BRDF kernels [44]

$$\rho(\theta_0, \theta_v, \phi, \lambda) = f_{\mathrm{iso}}(\lambda) + f_{\mathrm{vol}}(\lambda) K_{\mathrm{vol}}(\theta_0, \theta_v, \phi) + f_{\mathrm{geo}}(\lambda) K_{\mathrm{geo}}(\theta_0, \theta_v, \phi), \tag{5}$$

where $K_{\mathrm{vol}}(\theta_0, \theta_v, \phi)$ is known as the the Ross-thick kernel which parameterises *volumetric* scattering of leaves in dense vegetation and $K_{\mathrm{geo}}(\theta_0, \theta_v, \phi)$ is the Li-sparse kernel which parameterises *geometric* shadowing in sparsely wooded vegetation. The weights $f(\lambda)$ are provided by the 0.05° MODIS MCD43C1 BRDF auxiliary input discussed in section 3.

For the infrared channels the surface is assumed to have an emissivity of unity over the ocean, while the CIMSS global land emissivity database is used [37]. The temperature of the surface is a retrieved parameter (see section 2.3.8).

Each measurement pixel is considered to be either fully cloudy or clear. The algorithm does provide the capability of retrieving the cloud-filled fraction of a pixel, but it has been found that the heritage channels do not provide sufficient information to distinguish thin but complete cloud cover from thick but partial cover. Cloud is assumed to be a single, plane-parallel layer of either liquid or ice particles. The layer is assumed to be (geometrically) infinitely thin and is placed within the clear-sky atmosphere model. The cloud layer is parametrised in terms of the following retrieved quantities:

- The cloud phase, i.e. ice or liquid.
- The effective radius r_{eff} of the cloud particle size distribution.
- The total (vertically integrated) optical depth τ of the cloud at a fixed wavelength of 0.55 μm.
- The cloud top pressure p_{c}.

Size distributions for ice and liquid cloud are defined as a function of only r_{eff}, which defines the shape of the modelled size distribution, and τ, implicitly defining the total number of particles. For ice clouds, single-scattering properties (extinction coefficient, single-scattering albedo and phase function) are taken from Yang et al. [46]. A series of sensitivity tests have been conducted using the new ice habit models (i.e. solid columns, aggregates and a general habit mixture) and are described in the Supplementary Material [29]. Single-scattering properties of liquid cloud are derived by Mie theory assuming a modified gamma size distribution of particle radius r such that

$$n(r) = 2.373\, r^6 \exp\left(\frac{-6r}{r_m}\right), \tag{6}$$

where r_m is the mode radius of the distribution. The radiatively significant effective radius r_{eff} is given by

$$r_{\text{eff}} = \frac{\int_0^\infty r\pi r^3 n(r) dr}{\int_0^\infty \pi r^2 n(r) dr}. \tag{7}$$

This approach reduces the complexity of cloud to a simple model with parameters which can be distinguished using the heritage channels. The visible channel radiances are predominantly controlled by the cloud optical depth. Near-IR channels are also sensitive to particle size and phase due to the dependence on size of the single-scattering albedo in that spectral range and the associated differences between ice and liquid phase particles. Thermal channels predominantly provide information on cloud top pressure (via the dependence of the cloud thermal emission on the atmospheric temperature profile). It should be appreciated that all channels are sensitive, to a greater or lesser extent, to all parameters (dependant on the scene).

This simple model cannot represent all aspects of cloud three-dimensional structure. In the ideal case, the retrieved parameters should correspond to vertical (over the profile) and horizontal (over the scene) averages of the "true" cloudy properties. However, there are classes of clouds, particularly those with strong vertical variations in particle size and phase, for which this model cannot predict radiances consistent with observations in all channels. Such conditions can be identified by checking that the retrieval converges with satisfactory cost.

2.3.2 Reflectance and transmission operators

The next step in the forward model is the prediction of transmission and reflectance operators for an atmosphere *without* molecular absorption. This calculation is based on solar and viewing geometry, the molecular scattering optical thickness τ_{ms} and single-scattering phase function $P_{\text{ms}}(\lambda, \Theta)$, the optical thickness $\tau_{\text{a}}(\lambda)$, the single-scattering albedo $\omega_{\text{a}}(\lambda)$ and the single-scattering phase function $P_{\text{a}}(\lambda, \Theta)$. For performance reasons this calculation is look-up table (LUT) based from which the values for an arbitrary set of geometric and optical parameters may be interpolated (see Appendix C) . The vertices of the LUTs are computed with the DIscrete Ordinates Radiative Transfer (DISORT) software package [41]. It is important to note that this step, although slow, is performed off-line and the resulting look-up tables (LUTs) are static.

DISORT is a thoroughly documented and widely used general purpose algorithm for the calculation of time-independent radiative transfer. The DISORT algorithm solves the equation for the transfer of monochromatic light at wavelength λ in a medium with absorption and multiple scattering, including solar and thermal sources. The radiative transfer equation is written as

$$\mu \frac{dL_\lambda(\tau_\lambda, \mu, \phi)}{d\tau} = L_\lambda(\tau_\lambda, \mu, \phi) - J_\lambda(\tau_\lambda, \mu, \phi), \tag{8}$$

where $L_\lambda(\tau_\lambda, \mu, \phi)$ is the intensity along direction μ, ϕ (where μ is the cosine of the zenith angle and ϕ is the azimuth angle) at optical depth τ_λ measured perpendicular to the surface of the medium. $J_\lambda(\tau_\lambda, \mu, \phi)$ is the source function, which can include solar and thermal sources.

It should be noted that DISORT still makes some important approximations, which can limit its accuracy in certain circumstances. The most important of these are:

- It assumes a plane parallel atmosphere, which makes it inapplicable at viewing or zenith angles above approximately $75°$, where the curvature of the Earth has a significant influence on radiative transfer.
- It is a one-dimensional model, so cannot reproduce the effects of horizontal gradients in the scattering medium. This is important where strong gradients exist, such as near cloud edges.
- It does not model polarisation effects and hence cannot be used to model measurements made by instruments which are sensitive to polarisation and does not take into account the polarisation introduced into the diffuse component of radiance by molecular scattering.

DISORT is provided with solar and instrument geometry, the molecular scattering and cloud radiative properties at the vertexes. The transmission and reflectance of the atmosphere is computed for both direct beam and diffuse radiation sources separately. The calculations are performed quasi-monochromatically, i.e. a single radiative transfer calculation is performed for each channel. It is the input optical properties that are convolved to the instrument's response function for a particular channel. These calculations produce six LUTs for each channel:

- $R_{\mathrm{bb}}(\theta_0, \theta_\mathrm{v}, \phi)$: the bidirectional reflectance of the cloud.
- $T^{\downarrow}_{\mathrm{bb}}(\theta_0)$: the downward direct transmission of the cloud of the direct solar beam.
- $T^{\uparrow}_{\mathrm{bb}}(\theta_\mathrm{v})$: the upward direct transmission of the cloud into the viewing direction.
- $T^{\downarrow}_{\mathrm{bd}}(\theta_0)$: the downward diffuse transmission of the cloud, as illuminated by the direct solar beam.
- $T^{\uparrow}_{\mathrm{db}}(\theta_\mathrm{v})$: the upward diffuse transmission of the cloud, as viewed from a specific direction.
- R_{dd}: the bi-hemispherical reflectance of the cloud.

Here, a $\downarrow$ denotes transmission from the top to the bottom of the atmosphere, while $\uparrow$ indicates the reverse. Dependence on the solar zenith, viewing zenith and relative azimuth angles are denoted by θ_0, θ_v and ϕ respectively. The pairs of b and d subscripts denote the type of radiation each term operates on and produces; for example $T^{\downarrow}_{\mathrm{bd}}(\lambda, \theta_0)$ operates on the direct beam (b) of solar radiation, and produces the diffuse radiation (d) that results at the bottom of the atmosphere. Each of these tables contains tabulated transmission or reflectance (depending on the table) values for each of the ten equally spaced solar and/or sensor zenith angles, eleven equally spaced relative azimuth angles ($R_{\mathrm{bb}}(\lambda, \theta_0, \theta_\mathrm{v}, \phi)$ only), eighteen 0.55 μm optical depths and twenty three effective radii.

2.3.3 Surface reflectance operators

The CC4CL forward model works on the assumption that the surface BRDF can be parameterized by four reflectance terms:

1. The bidirectional reflectance, $\rho_{\mathrm{bb}}(\lambda, \theta_0, \theta_\mathrm{v}, \phi)$. This is the reflectance of the surface to direct beam illumination at θ_0, as viewed from a specific direction θ_v. It is the reflectance that would be observed by a satellite instrument in the absence of an atmosphere.

2. The directional-hemispheric reflectance $\rho_{\rm bd}(\lambda, \theta_0)$. This is the fraction of incoming direct beam illumination at θ_0 that is reflected across all viewing angles. This is also referred to as the *black-sky albedo*.

3. The hemispheric-directional reflectance $\rho_{\rm db}(\lambda, \theta_{\rm v})$. This is the reflectance of the surface to purely diffuse illumination, as viewed from a specific direction $\theta_{\rm v}$.

4. The bi-hemispheric reflectance $\rho_{\rm dd}(\lambda)$. This is the reflectance of the surface to purely diffuse illumination, across all viewing directions. This is also referred to as the *white-sky albedo*.

The first term $\rho_{\rm bb}(\theta_0, \theta_{\rm v}, \phi)$ is computed directly from the BRDF. The three other terms are derived from the BRDF integrated over solar and/or viewing geometry written as

$$\begin{aligned}\rho_{\rm bd}(\lambda, \theta_0) &= \frac{\int_0^{2\pi}\int_0^{\pi/2} \rho_{\rm bb}(\lambda, \theta_0, \theta_{\rm v}, \phi)\cos\theta_{\rm v}\sin\theta_{\rm v}{\rm d}\theta_{\rm v}{\rm d}\phi}{\int_0^{2\pi}\int_0^{\pi/2}\cos\theta_{\rm v}\sin\theta_{\rm v}{\rm d}\theta_{\rm v}{\rm d}\phi} \\ &= \frac{1}{\pi}\int_0^{2\pi}\int_0^{\pi/2}\rho_{\rm bb}(\lambda, \theta_0, \theta_{\rm v}, \phi)\cos\theta_{\rm v}\sin\theta_{\rm v}{\rm d}\theta_{\rm v}{\rm d}\phi,\end{aligned} \tag{9}$$

$$\begin{aligned}\rho_{\rm db}(\lambda, \theta_{\rm v}) &= \frac{\int_0^{2\pi}\int_0^{\pi/2} \rho_{\rm bb}(\lambda, \theta_0, \theta_{\rm v}, \phi)\cos\theta_{\rm v}\sin\theta_{\rm v}{\rm d}\theta_0{\rm d}\phi}{\int_0^{2\pi}\int_0^{\pi/2}\cos\theta_{\rm v}\sin\theta_{\rm v}{\rm d}\theta_0{\rm d}\phi} \\ &= \frac{1}{\pi}\int_0^{2\pi}\int_0^{\pi/2}\rho_{\rm bb}(\lambda, \theta_0, \theta_{\rm v}, \phi)\cos\theta_{\rm v}\sin\theta_{\rm v}{\rm d}\theta_0{\rm d}\phi,\end{aligned} \tag{10}$$

$$\begin{aligned}\rho_{\rm dd}(\lambda) &= \frac{\int_0^{\pi/2}\rho_{\rm bd}(\lambda, \theta_0)\cos\theta_0\sin\theta_0{\rm d}\theta_0}{\int_0^{\pi/2}\cos\theta_0\sin\theta_0{\rm d}\theta_0} \\ &= 2\int_0^{\pi/2}\rho_{\rm bd}(\lambda, \theta_0)\cos\theta_0\sin\theta_0{\rm d}\theta_0.\end{aligned} \tag{11}$$

2.3.4 Visible and near-IR RTM

Each short wave channel measures the radiance in the instrument's field-of-view, defined by the solid angle $\Delta_{\rm FOV}$. Each channel also has a relative spectral response $\varrho(\lambda)$ within a wavelength interval $[\lambda_1, \lambda_2]$ and has zero response outside this band. Under these conditions the radiance measured by the instrument is

$$L^r_{\bar{\lambda}}(\omega_r) = \frac{\int_0^{\Delta_{\rm FOV}}\int_{\lambda_1}^{\lambda_2} L^r_\lambda(\lambda, \omega)\varrho(\lambda)\,d\lambda\,d\omega}{\int_0^{\Delta_{\rm FOV}} d\omega}, \tag{12}$$

where ω is used to represent the spherical coordinate zenith and azimuth angle pair (θ, ϕ) and the integral over solid angle has been abbreviated as

$$\int_0^{\Delta\omega} d\omega \;=\; \int_0^{2\pi}\int_0^{\Delta\theta}\sin\theta\,d\theta\,d\phi. \tag{13}$$

The 'Sun-normalised radiance' (or top-of-atmosphere reflectance) can then be formed by dividing the measured radiance $L^r_{\bar{\lambda}}(\omega_r)$ by $E^0_{\bar{\lambda}}$, the irradiance the satellite would measure if viewing the Sun through a perfect diffuser i.e.

$$R(\bar{\lambda}, \omega_0, \omega_r) = \frac{\pi L^r_{\bar{\lambda}}(\omega_r)}{\cos\theta_0 E^0_{\bar{\lambda}}}. \tag{14}$$

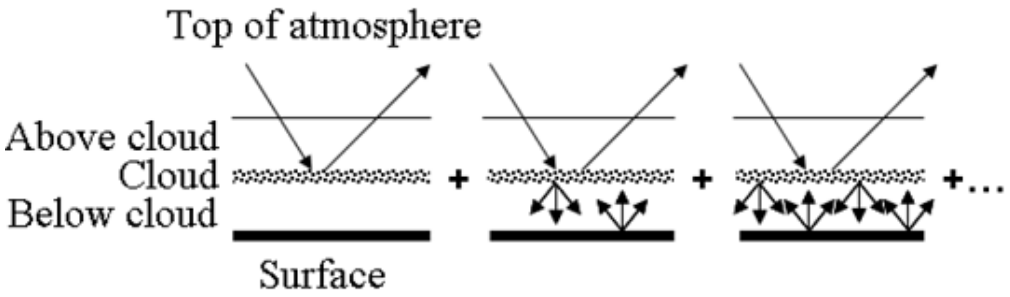

Figure 2: Schematic of the contributions to the measured radiance though multiple scattering between the atmosphere and surface.

The factor $\cos\theta_0$ accounts for the reduction in energy per unit area when the Suns energy strikes the atmosphere-Earth system at an angle θ_0 to the local vertical.

In the limit of a very narrow band, the measured Sun normalised radiance is a good approximation to the spectral bidirectional reflectance factor $R(\lambda, \omega_i, \omega_r)$, which is defined as the ratio of the reflected radiant flux to the reflected radiant flux from an ideal diffuse (i.e. Lambertian) surface [36]. The bidirectional reflectance factor is a function of the wavelength λ and the input and output directions (represented by ω_i and ω_r, respectively). For simplicity, the dependence of reflection and transmittance on λ will not be explicitly shown.

The cloudy fraction of the atmosphere in a scene is modelled with three layers: a below-cloud layer, a cloud layer and an above-cloud layer. The above and below-cloud layers consist of gaseous absorbers that attenuate radiation without scattering[3].

The gaseous absorption optical depth of the atmosphere is calculated using visible channel coefficients for RTTOV version 12.0 and the clear sky contribution for each scene is calculated with NWP information provided by 6-hourly ECMWF ERA Interim analyses. This total absorption optical depth is then partitioned into the above-cloud optical depth $\tau_{\rm ac}$ and the below-cloud optical depth $\tau_{\rm bc}$ based on the cloud top pressure relative to the surface pressure.

Using the reflectance and transmission operators described in section 2.3.2, the surface reflectance description in section 2.3.3, and by neglecting molecular absorption, the observed reflectance of the atmo-

[3]Molecular scattering throughout the atmospheric column is included in the scattering calculations carried out for the cloud layer

sphere/surface system can be written as (assuming dependence on wavelength λ):

$$
\begin{aligned}
R(\theta_0,\theta_\mathrm{v},\phi) = \; & R_\mathrm{bb}(\theta_0,\theta_\mathrm{v},\phi) && \}\text{Reflection off the atmosphere}\\
& +T^{\downarrow}_\mathrm{bb}(\theta_0)\rho_\mathrm{bb}(\theta_0,\theta_\mathrm{v},\phi)T^{\uparrow}_\mathrm{bb}(\theta_\mathrm{v}) && \\
& +T^{\downarrow}_\mathrm{bb}(\theta_0)\rho_\mathrm{bd}(\theta_0)T^{\uparrow}_\mathrm{db}(\theta_\mathrm{v}) && \Big\}\text{Single reflection off the surface}\\
& +T^{\downarrow}_\mathrm{bd}(\theta_0)\rho_\mathrm{db}(\theta_\mathrm{v})T^{\uparrow}_\mathrm{bb}(\theta_\mathrm{v}) && \\
& +T^{\downarrow}_\mathrm{bd}(\theta_0)\rho_\mathrm{dd}T^{\uparrow}_\mathrm{db}(\theta_\mathrm{v}) && \\
& +T^{\downarrow}_\mathrm{bb}(\theta_0)\rho_\mathrm{bd}(\theta_0)R_\mathrm{dd}\rho_\mathrm{db}T^{\uparrow}_\mathrm{bb}(\theta_\mathrm{v}) && \\
& +T^{\downarrow}_\mathrm{bb}(\theta_0)\rho_\mathrm{bd}(\theta_0)R_\mathrm{dd}\rho_\mathrm{dd}T^{\uparrow}_\mathrm{db}(\theta_\mathrm{v}) && \Big\}\text{Double reflection off the surface}\\
& +T^{\downarrow}_\mathrm{bd}(\theta_0)\rho_\mathrm{dd}R_\mathrm{dd}\rho_\mathrm{db}T^{\uparrow}_\mathrm{bb}(\theta_\mathrm{v}) && \\
& +T^{\downarrow}_\mathrm{bd}(\theta_0)\rho_\mathrm{dd}R_\mathrm{dd}\rho_\mathrm{dd}T^{\uparrow}_\mathrm{db}(\theta_\mathrm{v}) && \\
& +T^{\downarrow}_\mathrm{bb}(\theta_0)\rho_\mathrm{bd}(\theta_0)R_\mathrm{dd}\rho_\mathrm{dd}R_\mathrm{dd}\rho_\mathrm{db}T^{\uparrow}_\mathrm{bb}(\theta_\mathrm{v}) && \\
& +T^{\downarrow}_\mathrm{bb}(\theta_0)\rho_\mathrm{bd}(\theta_0)R_\mathrm{dd}\rho_\mathrm{dd}R_\mathrm{dd}\rho_\mathrm{dd}T^{\uparrow}_\mathrm{db}(\theta_\mathrm{v}) && \Big\}\text{Triple reflection off the surface}\\
& +T^{\downarrow}_\mathrm{bd}(\theta_0)\rho_\mathrm{dd}R_\mathrm{dd}\rho_\mathrm{dd}R_\mathrm{dd}\rho_\mathrm{db}T^{\uparrow}_\mathrm{bb}(\theta_\mathrm{v}) && \\
& +T^{\downarrow}_\mathrm{bd}(\theta_0)\rho_\mathrm{dd}R_\mathrm{dd}\rho_\mathrm{dd}R_\mathrm{dd}\rho_\mathrm{dd}T^{\uparrow}_\mathrm{db}(\theta_\mathrm{v}) && \\
& +\ldots &&
\end{aligned}
\tag{15}
$$

Here we have four terms resulting from a single surface reflection in equation 15, which can be described as follows:

- $T^{\downarrow}_\mathrm{bb}(\theta_0)\rho_\mathrm{bb}(\theta_0,\theta_\mathrm{v},\phi)T^{\uparrow}_\mathrm{bb}(\theta_\mathrm{v})$ is the direct transmission of the solar beam, reflected off the surface and transmitted directly to the satellite.
- In $T^{\downarrow}_\mathrm{bb}(\theta_0)\rho_\mathrm{bd}(\theta_0)T^{\uparrow}_\mathrm{db}(\theta_\mathrm{v})$ the diffusely reflected portion of the directly transmitted solar beam is diffusely transmitted (via multiple scattering in the atmosphere) into the viewing direction of the satellite.
- $T^{\downarrow}_\mathrm{bd}(\theta_0)\rho_\mathrm{db}(\theta_\mathrm{v})T^{\uparrow}_\mathrm{bb}(\theta_\mathrm{v})$ gives the portion of the diffusely transmitted solar beam, which is then reflected into the viewing direction of the satellite and directly transmitted back through the atmosphere.
- $T^{\downarrow}_\mathrm{bd}(\theta_0)\rho_\mathrm{dd}T^{\uparrow}_\mathrm{db}(\theta_\mathrm{v})$ is the purely diffuse component, where solar radiation is diffusely transmitted to the surface, reflected off the surface and diffusely transmitted to the satellite.

The terms following on from these describe the rapidly diminishing series of multiple reflections between the surface and overlaying atmosphere. For these terms the assumption has been made that ground and atmosphere pair are essentially Lambertian reflectors (i.e. that only the bi-hemispherical reflectance of the atmosphere is needed). Neglecting directly transmitted solar radiation, this is equivalent to saying the sky is equally bright in all directions.

By gathering terms, equation 15 can be simplified to give

$$
\begin{aligned}
R = \; & R_\mathrm{bb}(\theta_0,\theta_\mathrm{v},\phi) \\
& + T^{\downarrow}_\mathrm{bb}(\theta_0)\rho_\mathrm{bb}(\theta_0,\theta_\mathrm{v},\phi)T^{\uparrow}_\mathrm{bb}(\theta_\mathrm{v}) + T^{\downarrow}_\mathrm{bd}(\theta_0)\rho_\mathrm{db}(\theta_\mathrm{v})T^{\uparrow}_\mathrm{bb}(\theta_\mathrm{v}) \\
& + \left(T^{\downarrow}_\mathrm{bb}\theta_0)\rho_\mathrm{bd}(\theta_0) + T^{\downarrow}_\mathrm{bd}(\theta_0)\rho_\mathrm{dd}\right)T^{\uparrow}_\mathrm{db}(\theta_\mathrm{v})\left(1+\rho_\mathrm{dd}R_\mathrm{dd}+\rho^2_\mathrm{dd}R^2_\mathrm{dd}+\ldots\right) \\
& + \left(T^{\downarrow}_\mathrm{bb}(\theta_0)\rho_\mathrm{bd}(\theta_0) + T^{\downarrow}_\mathrm{bd}(\theta_0)\rho_\mathrm{dd}\right)R_\mathrm{dd}\rho_\mathrm{db}(\theta_\mathrm{v})T^{\uparrow}_\mathrm{bb}(\theta_\mathrm{v})\left(1+\rho_\mathrm{dd}R_\mathrm{dd}+\rho^2_\mathrm{dd}R^2_\mathrm{dd}+\ldots\right).
\end{aligned}
\tag{16}
$$

This can then be further simplified, using the appropriate series limit, to give

$$
\begin{aligned}
R = \; & R_\mathrm{bb}(\theta_0,\theta_\mathrm{v},\phi) \\
& + T^{\downarrow}_\mathrm{bb}(\theta_0)\rho_{bb}(\theta_0,\theta_\mathrm{v},\phi)T^{\uparrow}_\mathrm{bb}(\theta_\mathrm{v}) + T^{\downarrow}_\mathrm{bd}(\theta_0)\rho_\mathrm{db}(\theta_\mathrm{v})T^{\uparrow}_\mathrm{bb}(\theta_\mathrm{v}) \\
& + \frac{\left(T^{\downarrow}_\mathrm{bb}(\theta_0)\rho_\mathrm{bd}(\theta_0) + T^{\downarrow}_\mathrm{bd}(\theta_0)\rho_\mathrm{dd}\right)\left(T^{\uparrow}_\mathrm{db}(\theta_\mathrm{v}) + R_\mathrm{dd}\rho_\mathrm{db}(\theta_\mathrm{v})T^{\uparrow}_\mathrm{bb}(\theta_\mathrm{v})\right)}{1-\rho_\mathrm{dd}R_\mathrm{dd}}.
\end{aligned}
\tag{17}
$$

Finally, the observed TOA reflectance including molecular absorption is obtained by scaling the terms in equation 17 by the appropriate clear-sky transmission terms

$$
\begin{aligned}
R_{\mathrm{TOA}} = \mathcal{T}_{\mathrm{ac}}(\theta_0)\mathcal{T}_{\mathrm{ac}}(\theta_{\mathrm{v}}) \Big[& R_{\mathrm{bb}}(\theta_0, \theta_{\mathrm{v}}, \phi) \\
& + \mathcal{T}_{\mathrm{bc}}(\theta_0) T^{\downarrow}_{\mathrm{bb}}(\theta_0) \rho_{bb}(\theta_0, \theta_{\mathrm{v}}, \phi) T^{\uparrow}_{\mathrm{bb}}(\theta_{\mathrm{v}}) \mathcal{T}_{\mathrm{bc}}(\theta_{\mathrm{v}}) + \mathcal{T}_{\mathrm{bc}}(0) T^{\downarrow}_{\mathrm{bd}}(\theta_0) \rho_{\mathrm{db}}(\theta_{\mathrm{v}}) T^{\uparrow}_{\mathrm{bb}}(\theta_{\mathrm{v}}) \mathcal{T}_{\mathrm{bc}}(\theta_{\mathrm{v}}) \\
& + \frac{\left(\mathcal{T}_{\mathrm{bc}}(\theta_0) T^{\downarrow}_{\mathrm{bb}}(\theta_0) \rho_{\mathrm{bd}}(\theta_0) + \mathcal{T}_{\mathrm{bc}}(0) T^{\downarrow}_{\mathrm{bd}}(\theta_0) \rho_{\mathrm{dd}}\right) \left(\mathcal{T}_{\mathrm{bc}}(0) T^{\uparrow}_{\mathrm{db}}(\theta_{\mathrm{v}}) + R_{\mathrm{dd}} \mathcal{T}^2_{\mathrm{bc}}(0) \rho_{\mathrm{db}}(\theta_{\mathrm{v}}) T^{\uparrow}_{\mathrm{bb}}(\theta_{\mathrm{v}}) \mathcal{T}_{\mathrm{bc}}(\theta_{\mathrm{v}})\right)}{1 - \rho_{\mathrm{dd}} R_{\mathrm{dd}} \mathcal{T}^2_{\mathrm{bc}}(0)} \Big],
\end{aligned}
\tag{18}
$$

where $\mathcal{T}_{\mathrm{ac}}(\theta) = e^{-\tau_{\mathrm{ac}}/\cos\theta}$, $\mathcal{T}_{\mathrm{bc}}(\theta) = e^{-\tau_{\mathrm{bc}}/\cos\theta}$, τ_{ac} and τ_{bc} are the above cloud and below cloud optical thicknesses, respectively, and it is assumed that the mean angle of diffuse transmission is 66°.

2.3.5 Thermal-IR RTM

The thermal RTM makes extensive use of the RTTOV-12 model [32]. RTTOV directly provides the modelled radiance from the clear-sky fraction of the scene.

The observed cloudy brightness temperature is given by

$$
L^{\uparrow}(\theta_v) = L^{\uparrow}_{ac}(\theta_{\mathrm{v}}) + \left(L^{\downarrow}_{\mathrm{ac}} R^{\uparrow}_{\mathrm{db}}(\theta_{\mathrm{v}}) + B(T_{\mathrm{c}})\varepsilon_{\mathrm{c}} + L^{\uparrow}_{bc} T^{\uparrow}_{\mathrm{db}}(\theta_{\mathrm{v}})\right) e^{-(\tau_{\mathrm{ac}}/\cos\theta_{\mathrm{v}})}, \tag{19}
$$

where $L^{\uparrow}_{ac}(\theta_{\mathrm{v}})$ is the upward radiance into the viewing direction from the atmosphere above the cloud, $L^{\downarrow}_{ac}$ is the downward radiance from the atmosphere above the cloud, $L^{\uparrow}_{bc}$ is the upward radiance from the atmosphere below the cloud, $B(T_{\mathrm{c}})$ is the Planck function as a function of the cloud top temperature T_{c}, ε_{c} is the cloud emissivity obtained from an LUT computed in a similar way as those for the operators R and T and $e^{-(\tau_{\mathrm{ac}}/\cos\theta_{\mathrm{v}})}$ is the transmission from TOA to the cloud top. The transmission term $e^{-(\tau_{\mathrm{ac}}/\cos\theta_{\mathrm{v}})}$ is obtained from transmission profiles computed with RTTOV while the clear-sky radiance terms L are obtained from thermal emission profiles computed with RTTOV.

2.3.6 Derivatives of the forward model

The gradient of the forward model $\partial y_i/\partial x(j$, where y_i is a radiance measurement in a single channel and x_j is one of the retrieved parameters, is required for the following purposes:

1. The gradient with respect to parameters which are to be derived from the measurements (state parameters) is a vital quantity for the inversion of the non-linear reflectance model by the Levenberg-Marquardt algorithm.

2. The gradient with respect to parameters which might be considered known and not part of the inversion procedure (model parameters such as surface reflectance spectral shape) is used to judge the sensitivity to these parameters and thus to estimate their contribution to the retrieval uncertainty.

Derivatives of the forward model may be obtained through straightforward linearisation of the forward model equations already given and as a result will not be listed here.

2.3.7 Single layer Measurement vector and covariance

The retrieval scheme described here uses nadir-view observations in the 0.67, 0.87, 1.6, 3.7, 11 and 12 μm channels. In practice only one of the 1.6 or 3.7 μm channels is included in a given retrieval because it has been

found to be difficult to consistently represent both the 1.6 and 3.7 μm channels with the simple CM used [3]. Similarly, forward view radiances are not included as the three-dimensional structure of cloud will often cause differences between the views which cannot be accommodated by the simple model. The error covariance used in the retrieval is the sum of three terms:

$$\mathbf{S}_y = \mathbf{S}_{\text{noise}} + \mathbf{S}_{\text{pixel}} + \mathbf{S}_{\text{fm}}. \tag{20}$$

- $\mathbf{S}_{\text{noise}}$ represents random instrument noise on the observations. The matrix is assumed diagonal with values on the diagonal equal to the square of the assumed measurement noise, which are set for each instrument based on pre-launch characterisation.

- $\mathbf{S}_{\text{pixel}}$ represents errors related to inadequacies of the plane-parallel cloud model and imperfect co-registration of the channels. It is assumed diagonal and equal to the square of 2 % of the measured radiance for visible and near-IR channels[4]. and 0.08 K for the thermal channels. These are combined for the mixed 3.7 μm channel[5]. See Watts et al. [45] for the derivation of this term.

- $\mathbf{S}_{\text{fm}}$ is zero for rows and columns corresponding to thermal channels. For the visible and near-IR channels, the matrix represents uncertainties in the MODIS surface albedo. Diagonal elements are set to (the square of) 20 % of the albedo for the corresponding channel. Off-diagonals are set to give a correlation between the visible/near-IR channels of 0.2.

2.3.8 State vector and a priori constraint

The state-vector used in the retrieval prescribes:

- Log_{10} optical depth;
- Cloud effective radius;
- Cloud top pressure;
- Surface temperature.
- Cloud fraction

A priori and first guess values depend on the assumed phase (phase determination is addressed in section 2.2 and section D.2). For liquid cloud, *a priori* values are 6.3, 12 μm and 900 hPa for optical depth, effective radius and cloud top pressure, respectively; for ice the equivalent values are are 6.3, 30 μm and 400 hPa. The surface temperature *a priori* value is taken from ECMWF reanalysis fields for the skin temperature. Currently the cloud fraction is not retrieved as it was found that allowing the cloud fraction to vary introduced compensating effects. However in the future if subpixel cloud fraction was available with improved confidence this could be easily reintroduced. A more complete exploration of the sea surface temperature retrieval can be found in **(author?)** [Cox et al].

In the absence of useful information, the *a priori* uncertainty for the state parameters is set to 10^8 for optical depth, effective radius, and cloud top pressure. This implies that these parameters are effectively unconstrained by their *a priori* value. For surface temperature, the *a priori* uncertainty is set to 2 K over sea and 5 K over land. The *a priori* covariance is assumed to be diagonal.

The initial (first guess) values for state-vector parameters are set equal to the *a priori* values, except cloud top pressure which is set by:

[4]For ATSR-2 channel 4, the visible uncertainty is 1.5 %.

[5]For mixed channels, the radiance is converted into an equivalent brightness temperature.

- Find the channel with wavenumber less than 2500 cm^{-1} that is nearest to 909 cm^{-1}. If there is no such channel, do not attempt a retrieval.
- Convert the brightness temperature in that channel to a radiance. If the pixel is flagged as clear, subtract the TOA clear-sky radiance (as given by the LUT for that channel).
- If that radiance is less than zero, use the first guess specified above. Otherwise, convert the radiance into a brightness temperature and interpolate it onto the ECMWF temperature profile to find the first guess cloud top pressure.

2.3.9 Cloud Emissivity and microphysical retrievals at night and twilight

The retrieval of cloud top height typically relies on matching thermal emission from a cloud in the 11μm window to a vertical location in a known temperature profile. Without accounting for cloud transparency, this method produces heights that are biased low for semi-transparent clouds due to the contribution of thermal emission from below the cloud. Including additional thermal channels allows for the possibility of retrieving information on cloud transparency from which it is possible to separate the cloud from the below-cloud signal. In particular, the 3.7-μm channel paired with 11 μm has been used to retrieve cloud top height along with a single microphysical parameter that describes the cloud radiative thickness in the infrared, typically referred to as the "effective emissivity". In a similar manor it has been shown that the relative interdependence of optical thickness and effective radius in the 3.7 and 11.0μm combination allows these to be retrieved along with cloud top pressure, although with a significantly greater uncertainty than using solar wavelengths during the day.

The night retrieval is run where the solar zenith angle is greater than 90° or at least two visible/near-IR channels do not convey valid information. Twilight conditions are defined by solar zenith angles between 80° and 90°, where the 3.7 μm channel is not used due to solar contamination. Retrievals in Twilight conditions are performed however the quality is poor due to the difficulty in modelling the solar contribution of the 3.7μm channel.

2.3.10 Cloud Albedo

Given the reflection function is parameterised as a function of waveband, input and output geometry and cloud properties (optical depth, effective radius and phase), it is possible to output three reflection terms:

- The cloud reflection factor for the Sun-cloud-satellite geometry $R(\mu_0, \phi_0; \mu, \phi)$;
- The directional-hemispherical reflectance for unidirectional illumination (also called the black-sky albedo)

$$R(\mu_o) = \frac{1}{\pi} \int_0^{2\pi} \int_0^1 R(\mu_0, \phi_0; \mu, \phi) \mu \, d\mu \, d\phi; \tag{21}$$

- The cloud bihemispherical reflectance for isotropic illumination (also called the white-sky albedo)

$$R = \frac{1}{\pi^2} \int_0^{2\pi} \int_0^1 \int_0^{2\pi} \int_0^1 R(\mu_0, \phi_0; \mu, \phi) \mu \, d\mu \, d\phi \, \mu_0 \, d\mu_0 \, d\phi_0. \tag{22}$$

Note that these terms are calculated in the absence of knowledge of the underlying surface so they refer to a cloud property alone.

The black-sky albedo is currently the reported cloud albedo in the CCI product.

2.3.11 Corrected CTT, CTP and CTH

The temperature of the geometric top of the cloud, which we have named as the *corrected* cloud top temperature $T_{\mathrm{c,cor}}$, in contrast to the retrieved radiative cloud top temperature T_{c} (CTT), may be written as

$$T_{\mathrm{c,cor}} = \mathrm{BT_c}(\lambda) + \Gamma \Delta Z, \tag{23}$$

where $\mathrm{BT_c}(\lambda)$ is the brightness temperature (K) at wavelength λ observed from the *top of the cloud*, Γ is the atmospheric lapse rate (-K/km) and ΔZ (km) is the geometric depth into the cloud of T_{c}.

If we assume that the cloud is vertically homogeneous the cloud optical depth $\Delta\tau_{\mathrm{c}}(\lambda)$ at a geometric depth ΔZ (km) into the cloud is given by

$$\Delta\tau_{\mathrm{c}}(\lambda) = \sigma_{\mathrm{c}}(\lambda) N_{\mathrm{c}} \Delta Z, \tag{24}$$

where $\sigma_{\mathrm{c}}(\lambda)$ is the size distribution averaged cloud particle cross section and N is the cloud particle number concentration ($1/\mathrm{km}^3$). If we assume that the peak sensitivity to T_{c} comes from one optical depth into the cloud ($\Delta\tau_{\mathrm{c}} = 1$) then ΔZ may be written as

$$\Delta Z = \frac{1}{\sigma_{\mathrm{c}}(\lambda) N_{\mathrm{c}}}. \tag{25}$$

From equation 23, two equations may be formed, for measurements at 11 and 12 , respectively:

$$T_{\mathrm{c,cor}} = \mathrm{BT_c}(11) + \frac{\Gamma}{\sigma_{\mathrm{c}}(11) N_{\mathrm{c}}}, \tag{26}$$

$$T_{\mathrm{c,cor}} = \mathrm{BT_c}(12) + \frac{\Gamma}{\sigma_{\mathrm{c}}(12) N_{\mathrm{c}}}, \tag{27}$$

where there are two unknowns, $T_{\mathrm{c,cor}}$ and Γ/N_{c}. By solving for Γ/N_{c} with each equation and equating the results as

$$\sigma_{\mathrm{c}}(11)\left[T_{\mathrm{c,cor}} - \mathrm{BT_c}(11)\right] = \sigma_{\mathrm{c}}(12)\left[T_{\mathrm{c,cor}} - \mathrm{BT_c}(12)\right], \tag{28}$$

$T_{\mathrm{c,cor}}$ may be solved for, given by

$$T_{\mathrm{c,cor}} = \frac{\sigma_{\mathrm{c}}(11)\mathrm{BT_c}(11) - \sigma_{\mathrm{c}}(12)\mathrm{BT_c}(11)}{\sigma_{\mathrm{c}}(11) - \sigma_{\mathrm{c}}(12)}. \tag{29}$$

The brightness temperatures as observed from the top of the cloud, $\mathrm{BT_c}(\lambda)$ may be obtained from the corresponding brightness temperatures observed at TOA $\mathrm{BT_{TOA}}(\lambda)$ with

$$\mathrm{BT_c}(\lambda) = \mathrm{BT_{TOA}}(\lambda)/\mathcal{T}_{\mathrm{ab}}(\lambda), \tag{30}$$

where $\mathcal{T}_{\mathrm{ab}}(\lambda)$ is the above cloud clear-sky atmospheric transmittance, i.e. the transmittance from TOA to the top of the cloud, along the satellite viewing slant path. Cloud particle cross section $\sigma_{\mathrm{c}}(\lambda)$ is obtained from pre-computed LUTs as a function of wavelength and the retrieved cloud optical thickness (COT) and cloud effective radius (CER).

The corresponding corrected cloud top pressure $P_{\mathrm{c,cor}}$ and corrected cloud top height $H_{\mathrm{c,cor}}$ may be obtained from the input pressure and temperature profiles simply by comparing $T_{\mathrm{c,cor}}$ with the input temperature profile and interpolating appropriately.

The estimated uncertainties of $T_{\mathrm{c,cor}}$, $P_{\mathrm{c,cor}}$ and $H_{\mathrm{c,cor}}$ are obtained through straight forward error propagation, the details of which will not be discussed here.

2.3.12 Cloud condensation nuclei

Cloud droplet number concentration (CDNC) is an increasingly frequently used quantity in the study of aerosol-cloud interactions as it reflects the microphysical processes by which anthropogenic aerosols can affect cloud properties. Section 2.1 of Grosvenor et al. [12] outlines how it can be estimated from a cloud's optical depth and effective radius by,

$$N_d = \frac{1}{2\pi k}\sqrt{\frac{5 f_{ab} c_w \tau_c}{Q_{ext}\rho_w r_e^5}}, \tag{31}$$

where k is the assumed[6] value of the ratio $(r_v/r_e)^3$ for volume-mean radius r_v and effective radius r_e; f_{ab} is the assumed[7] ratio between liquid water content and its adiabatic value; c_w is the condensation rate of water; τ_c is the cloud optical depth; $Q_{ext} = 2$ is the extinction factor of small droplets; and ρ_w is the density of water.

Following Gryspeerdt, Quaas and Bellouin [13], c_w is assumed to be constant such that,

$$N_d = 1.37 \times 10^{-11} \tau_c^{0.5} r_e^{-2.5}. \tag{32}$$

Use of a CDNC product requires careful quality control as the assumptions are mostly appropriate for stratocumulus cloud, where N_d has been observed to be largely constant with height. Gryspeerdt, Quaas and Bellouin [13] requires that:

- Cloud phase is liquid water;
- Cloud top temperature is greater than 268 K;
- The cloud has not been flagged as multilayer;
- Solar zenith angle is less than $65°$;
- Satellite zenith angle is less than $41.4°$;
- Cloud_Mask_SPI, the ratio of standard deviation to mean in the 250 m visible channels to measure of sub-pixel heterogeneity, is less than 10% (though 30% is also acceptable if the volume of data is too small).

All but the last of these is adopted here and the heterogeneity product is expected to be implemented for SLSTR later in this project.

2.3.13 Cloud physical thickness

The physical thickness of the cloud can be deduced using the same assumptions as the CDNC above. The liquid water content l at the top of a cloud with depth H is,

$$l(H) = f_{ab} c_w H = \frac{4}{3}\pi \rho_w k N_d r_e^3. \tag{33}$$

Substituting for $(\pi k N_d)^2$ in Eq. 31 and rearranging for H gives,

$$H = \sqrt{\frac{20 \rho_w \tau_c r_e}{9 Q_{ext} f_{ab} c_w}}. \tag{34}$$

This was first published as Eq. 4 in Meerkötter and Zinner [23].

[6] This ratio being constant follows from the droplets conforming to a modified gamma distribution; values between 0.67 and 0.88 have been used.

[7] This varies between 0.1 and 0.9, commonly assumed to be 0.66.

2.3.14 Boundary layer inversion

A boundary layer temperature inversion can often permit two valid solutions for the cloud top pressure within the OEM retrieval, depending on whether one searches the temperature profile from top to bottom or vice versa. Thus, the retrieved height may either be too high or too low. The following solution is derived from the Meteosat Third Generation Level 2 Processing Specification Document [25] but is repeated here as that document is not easily accessible:

- Search from the bottom of the forecast temperature profile for a typical anticyclonic temperature inversion. Numbering the levels of the forecast model from 1 at the surface to N at TOA, an inversion is identified by the smallest $1 < i < N$ where $T^i_{\text{fcst}} < T^{i+1}_{\text{fcst}} - 1\,\text{K}$ and $T^i_{\text{fcst}} < T^{i-1}_{\text{fcst}}$ with $P^i_{\text{fcst}} > 600\,\text{hPa}$ (where T^i_{fcst} and P^i_{fcst} are the temperature and pressure at forecast level i, respectively). Eventually, this scheme should be extended to account for the humidity profile.

- The top of the inversion is identified as the smallest $j \geq i + 2$ at which $T^j_{\text{fcst}} < T^{j-1}_{\text{fcst}}$.

- If no inversion is found, the forecast temperature profile is retained. Otherwise, modify the temperature profile within the inversion to facilitate a more sensible cloud top pressure retrieval. This extrapolates the boundary layer below the inversion such that:

$$T^k = \begin{cases} T^i_{\text{fcst}} + \Gamma_{\text{BL}} \left(P^k_{\text{fcst}} - P^i_{\text{fcst}} \right) & i < k \leq j + 2 \\ T^k_{\text{fcst}} & \text{otherwise,} \end{cases} \tag{35}$$

  where the boundary layer lapse rate Γ_{BL} is approximated from the levels beneath the inversion,

$$\Gamma_{\text{BL}} = \frac{\mathrm{d}T}{\mathrm{d}P} \simeq \frac{T^{i-1}_{\text{fcst}} - T^{i-2}_{\text{fcst}}}{P^{i-1}_{\text{fcst}} - P^{i-2}_{\text{fcst}}}. \tag{36}$$

- The $+2$ in eqn. 35 and the second step account for uncertainty in the bounding of the inversion due to forecast model errors and smoothing.

2.3.15 Tropopause identification and temperature profile modification

Occasionally deep convective clouds rise above the tropopause and there is a delay before this is expressed in the temperature profile. If not corrected, the retrieved cloud top height will be too low. This is accounted for, equivalent to Section 2.3.14, by extrapolating from the temperature profile just below the tropopause:

- The tropopause is identified by the largest $i < N$ where $T^i > T^{i+1}$, $T^{i-2} - T^{i-1} > 2\,\text{K}$ and $P^{i+1}_{\text{fcst}} > 80\,\text{hPa}$.

- The temperature profile is then modified such that:

$$T^k_{\text{modified}} = \begin{cases} T^i + \Gamma_{\text{troposphere}} \left(P^k_{\text{fcst}} - P^i_{\text{fcst}} \right) & i < k \leq N \\ T^k & \text{otherwise,} \end{cases} \tag{37}$$

  where the tropospheric lapse rate $\Gamma_{\text{troposphere}}$ is approximated from the levels beneath the tropopause,

$$\Gamma_{\text{troposphere}} = \frac{T^{i-2}_{\text{fcst}} - T^i_{\text{fcst}}}{P^{i-2}_{\text{fcst}} - P^i_{\text{fcst}}}. \tag{38}$$

2.3.16 1.38 μm channel cloud detection and height estimation

A spectral channel centred near 1.38 μm is provided on some instruments, most notably for CC4CL on Sentinel-3 SLSTR, in order to aid detection of high-altitude, optically thin clouds. This wavelength corresponds to a strong atmospheric water-vapour absorption line – which minimises the surface reflectance and lower-atmosphere signal due to strong attenuation of the signal in the troposphere – while cloud water droplets and ice crystals are highly reflective in the near-IR. Thus, high altitude clouds are generally the only bright features apparent in TOA measurements made at this wavelength.

However, the dependence of the radiance observed in this channel to water-vapour concentration makes its use in a the CC4CL retrieval difficult, as the accurate forward modelling of the TOA radiance relies on the accuracy of the prior water-vapour profile. Thus, the approach taken to utilising the information provided by a 1.38 μm observation in ORAC is not to include the channel in the retrieval itself, but to use it to define a prior estimate of cloud-top pressure, which can then be used as a cloud-mask modifier and/or cloud-top pressure a priori and/or first-guess. The creation of a module to provide this prior was governed by the following criteria:

- The module should provide an estimate of cloud-top pressure, along with a reasonable estimate of the pixel-by-pixel uncertainty.
- Dependence on additional ancillary information and data should be minimised. Ideally only the data provided by the standard preprocessing should be needed.
- Additional computational overhead should be minimised.

The RTM calculations performed by the pre-processing (see section 2.3.17) provide the expected absorption of 1.38 μm radiation throughout the atmospheric column, $\beta^{\rm abs}_{1.38}(z)$, where z denotes dependence on height or, equivalently, atmospheric pressure. If we are able to estimate the TOA 1.38 μm in the absence of any water vapour absorption, $R^{\rm dry}_{1.38}$, we can then use $\beta^{\rm abs}_{1.38}(z))$ to simulate the observed TOA 1.38 μm reflectance, $R^{\rm TOA}_{1.38}$. Positioning our reflecting surface (aka cloud) at different heights within our $\beta^{\rm abs}_{1.38}(z))$ profile, allows us to determine which pressure level best reproduces $R^{\rm TOA}_{1.38}$. The unknown quantity in this approach is $R^{\rm dry}_{1.38}$, which is function of the surface reflectance, viewing geometry, properties of any cloud present and (to a lesser extent) the profiles of other atmospheric constituents. In the case of SLSTR, we make the assumption that the adjacent 1.6 μm channel, which has a much lower water vapour absorption, can be used as a proxy for the 1.38 μm TOA reflectance in the absense of water vapour:

$$R^{\rm dry}_{1.38} \approx R^{\rm TOA}_{1.6}. \tag{39}$$

Thus, the estimation of cloud-top height (or, equivalently, pressure) becomes the simple matter of finding the minimum of the function:

$$\mid R^{\rm TOA}_{1.38} - 2R^{\rm TOA}_{1.6} \int_z^{\rm TOA} \beta^{\rm abs}_{1.38}(z){\rm d}z \mid, \tag{40}$$

where $R^{\rm TOA}_{1.38}$ and $R^{\rm TOA}_{1.6}$ are SLSTR observations, and $\int_z^{\rm TOA} \beta^{\rm abs}_{1.38}(z){\rm d}z$ is tabulated in the pre-processor RTM output.

The most computationally intensive aspect of this calculation is the interpolation of the $\int_z^{\rm TOA} \beta^{\rm abs}_{1.38}(z){\rm d}z$ profiles, which are stored on the 0.5° lat-lon pre-processing grid, onto the SLSTR level-1 pixel grid. This is performed using bilinear interpolation onto the SLSTR level-1 lat-lon grid (in the same way as is done by the CC4CL processor itself).

In addition, the SLSTR observations of $R^{\rm TOA}_{1.38}$ have been found to suffer from anomalies, where isolated pixels have very low reflectances which are not contiguous with neighbouring pixels and are well below the noise threshold of the instrument itself. Such pixels are effectively removed from the observations by running

a 5×5 pixel median filter over $R_{1.38}^{\mathrm{TOA}}$, with a corresponding degradation of spatial resolution.

Uncertainty estimation

There are several sources of uncertainty in the estimation of height or pressure from this method, the relative importance of which will vary from pixel to pixel:

1. The noise in the $R_{1.38}^{\mathrm{TOA}}$ and $R_{1.6}^{\mathrm{TOA}}$, which are taken to be $\sigma = 3.4\%$ and 2.8% respectively, based on pre-launch calibration Etxaluze and Smith [11].
2. Uncertainty in the $\int_z^{\mathrm{TOA}} \beta_{1.38}^{\mathrm{abs}}(z)\mathrm{d}z$ calculated from reanalysis data.
3. Errors introduced by the neglect of the spectral dependence of cloud reflectance between 1.38 and 1.6 μm.
4. The assumption that the observed reflectance corresponds to the cloud-top (i.e. neglecting the volumetric multiple scattering which actually governs the reflectance of clouds and the transmission radiance from below the cloud).

The first of these uncertainties is well quantified and the uncertainties in observed radiance can be propagated into uncertainty in cloud-top height using standard linear error propagation:

$$(\sigma_z)^2 = \left(\frac{\mathrm{d}z}{\mathrm{d}R_{1.38}^{\mathrm{est}}}\right)^2 (\sigma_{1.38}^2 + \sigma_{1.6}^2), \tag{41}$$

where σ_z is the 1-sigma error on the derived height (or pressure), $\frac{\mathrm{d}z}{\mathrm{d}R_{1.38}^{\mathrm{est}}}$ is the derivative of z wrt to a change in estimated 1.38 μm reflectance, $R_{1.38}^{\mathrm{est}} = \int_z^{\mathrm{TOA}} \beta_{1.38}^{\mathrm{abs}}(z)\mathrm{d}z$. $\sigma_{1.38}$ and $\sigma_{1.6}$ are the noise values of the two channels.

The other components of the uncertainty are harder to quantify and, at present, are estimated as a constant uncertainty of 1 km in cloud-top height, or 10% in cloud-top pressure.

Cloud detection

This aspect of the use of a 1.38 μm measurement has yet to be included into ORAC. However, a simple methodology, which builds on the existing cloud-top pressure calculation would be to simply set a thresholds on the uncertainty of 1.38 μm derived cloud-top height or pressure, as well as on altitude above the surface. Observations that pass each of these threshold would be identified as cloud and the existing cloud-mask defined in the standard pre-processing modified, if not already flagged as cloud.

I should be noted that, due to its low sensitivity to the lower atmosphere, the 1.38 μm reflectance can only be used to conclusively detect cloud - it cannot be used to flag pixels as cloud-free.

Incorporation into the CC4CL processing chain

The 1.38 μm module is designed too run between the pre-processing and main retrieval steps. The module reads the "msi" (satellite TOA reflectances/brightness temperatures), "loc" (level-1 pixel lat-lon grid), "swrtm" (RTM output for shortwave channels), and "prtm" (RTM lat-lon grid and height, temperature, humidity and ozone profiles) files produced by the pre-processing.

The output consists of a NetCDF file, similar in format to the pre-processing output files, which contains (at minimum) variables named "ctp", containing the estimated cloud-top pressure for each level-1 pixel, and "ctp_var" containing the *variance* defining the uncertainty of the height estimate for each pixel. Any pixels with no valid cloud-top pressure value should have a fill-value assigned (with the corresponding "_fillvalue" variable attribute also defined).

If the retrieval is called with the "Ctrl%FG(IPc,1) = SelmAux" option specified in the driver file, the values of the 1.38 μm based cloud-top pressure are used as the first guess in the OE retrieval. Similarly, setting "Ctrl%AP(IPc,1) = SelmAux" sets the a priori cloud-top pressure using the 1.38 μm derived values, with the uncertainty variance values used to define a diagonal a priori covariance matrix.

2.3.17 ECMWF data

Clear-sky atmospheric radiances and transmittances are determined by RTTOV. This requires meteorological information as an input, which is provided by ECMWF ERA5 reanalysis fields [15]. The required data[8] are stored in one or more files of NetCDF or GRIB format. The data presents values and profiles representative of the atmosphere and surface at each point on a regular 0.5° degree latitude-longitude grid. ORAC retrieves states averaged over each satellite pixel and, to reduce computational expense, only evaluates RTTOV on a regular 500-by-500 latitude-longitude grid, which is then linearly interpolated onto each satellite pixel. (The errors from this process have been found to be less than the uncertainties in the RTTOV calculations themselves and so are considered negligible.)

The ECMWF data must be interpolated onto the ORAC grid. As the ECMWF data is generally on a coarser grid than that used by ORAC, the grid-cell average is approximated by the ECMWF value at the cell centre. The interpolation is performed using the EMOSLIB library provided by ECMWF (found at `software.ecmwf.int/wiki/display/EMOS/Emoslib`).

2.3.18 Quality Control

The quality of the ORAC algorithm is based on the output diagnostics of the OE retrieval.

- The number of iterations: Indicates if the retrieval has converged.
- A convergence test: ORAC uses the change in the cost function between iterations to determine whether a retrieval has converged.
- Cost function: If the cost function is approximately equal to the number of measurements then the retrieval is thought to have fit the model well. In practice, any retrieval with cost greater than ten times the number of measurements is considered suspect.
- Error estimates: If the previous criteria is satisfied then the uncertainty on the retrieved parameters is given in the solution covariance.

2.3.19 Aerosol-Cloud (and sunglint) discrimination

Evaluation have shown that occasionally heavy aerosol loading are misclassified as clouds. Two empirical reclassification approaches have been developed and applied.

1. Removal of clouds over the Sahara region if: (i) the total cldmask_uncertainty (which is the sum of both views when used from AATSR) is greater then 70 and (ii) the Pavolonis cloud type is water (in either view in case of AATSR two views retrievals).
2. Removal of clouds based on combined testing of (i) the 11µm-12µm brightness temperature difference (being between 0 and 3K), (ii) the Brightness temperature in 11µm being larger than 290K and (iii) the spatial (in-)homogeneity in the 11µm channel (standard deviation in 3x3 pixels) being smaller 0.25K. If all of these requirements are fulfilled the pixel is reclassified as clear-sky in case it was classified as cloudy beforehand. The cloud mask uncertainty is set to 99% in such pixels.

[8] Currently, the fields `temperature`, `spec_hum`, `ozone`, `geopot`, `lnsp`, `sea_ice_cover`, `snow_albedo`, `sst`, `totcolwv`, `snow_depth`, `u10`, `v10`, `temp2`, `land_sea_mask` and `skin_temp` are required.

2.4 Retrieval Performance

For a comprehensive evaluation of the retrieval performance the reader is reffered to [22] [PVIR] and [40]. The results are briefly summarised here. The performance of the retrieval method was assessed theoretically by simulating measurements using a range of values for the retrieval parameters and then subsequently performing a retrieval on these simulated measurements to which Gaussian noise levels appropriate for MODIS were added. The errors are less than 10% for optical thicknesses larger than 10 and less than 20% for optical thicknesses larger than unity. For optical thicknesses less than unity the results become problematic, which could have implications for the retrieval of subvisible cirrus. When the algorithm is run in 'heritage' mode the cloud top height for multi layer cloud systems with a thin (less than 4 COT) is located between the upper and lower layer at the radiative cloud top height. The cloud fraction has been validated for different cloud regimes and found to perform well over sea and target surfaces with performance reduced over the polar regions.

2.5 Changes compared to precursor CC4CL version

Between ATBDv5.1 (describing CC4CL as used for dataset versions 2) and the version used for dataset version 3 and the current test processing of SLSTR and SEVIRI a number of changes and significant bug fixes were made to the retrieval algorithm, which are listed in the following.

Changes applying to the processing of both AVHRR and ATSR2-AATSR:

- Retraining ANN for cloud detection incorporating a much larger data basis and with the emphasis on NOAA-19 AVHRR. Furthermore, new channel settings for ANN input, new scene dependent thresholds for deriving binary cloud mask, new spectral band adjustment to make all sensors mimic NOAA-19 AVHRR.

- Introduction of a ANN for phase identification with a very similar approach as for cloud detection, also using CALIOP phase as truth. By this cloud phase uncertainty is introduced as well, derived in a similar manner as for cloud detection. Cloud typing remains to be based on Pavolonis schemes.

- Implementing BRDF calculation bug fix, in particular improving retrievals in polar regions

- Using a spatially higher resolved land/sea mask dataset (USGS 0.5km MODIS based Land Cover Type 2 data)

- A comprehensive review of ice optical properties was undertaken and a new set of forward model LUTs based on Baum [46] optical properties where derived that show improved results, most significantly for cloud ice effective radius (and ice water path).

- New QC information regards sunglint and surface type (e.g. ice and snow), and includes a simplified high quality/low quality flag meant for general users.

- Including BUGSRAD scheme for calculation of radiative broadband fluxes at top of atmosphere and surface (bottom of atmosphere). See CC4CL TOA FLUX ATBD (available at http://www.esa-cloud-cci.org/?q=documentation) for details.

- Implemented time dependent CO_2 in RTTOV and BUGSRAD calculations.

3 Input and output data

The primary input data used by CC4CL are calibrated, geolocated satellite radiances, generally referred to as level 1 data.

- When applied to SLSTR, CC4CL ingests standard level 1 data from either collection 3 or 4, as defined the Sentinel-3 Product Data Format Specification [1].
- SEVIRI input data are L1B data in the so called High Rate Information Transmission (HRIT) format as defined in the MSG Level 1.5 Image Data Format Description [10].

The physical quantity measured by satellite radiometers is radiance. Two modifications are made to the radiance for use with CC4CL: the shortwave channels are scaled by the cosine of the solar zenith angle and normalised, to produce a sun-normalised reflectance, and the thermal channel radiances are converted to brightness temperatures in Kelvin.

These files then provide CC4CL with:

- Calibrated TOA reflectance/brightness temperature;
- Solar and satellite azimuth and zenith angles;
- A land/sea mask for the level 1 grid.

CC4CL also makes use of a range of ancillary data:

- ECMWF ERA-5 humidity and temperature profiles, total column ozone, surface temperature and pressure, and 10 m east-west and north-south (u and v) wind components. These are used by the sea surface reflectance model to determine surface roughness and whitecap coverage and to estimate the sea surface emissivity.
- to ensure historical consistency ECMWF snow/mask can be used, while an option has been implemented to use higher resolution snow masks (e.g. NISE). The snow/ice information is used to modify the surface albedo and BRDF calculations.
- MODIS MCD43C1 surface BRDF product produced daily with a 16-day acquisition period from combined Aqua and Terra-based MODIS observations [19, 35].
- The emissivity over land is taken from the CIMSS database [37]. Optional is the utilization of an ancillary land/sea mask, overwriting land/sea information contained in L1 data. This option has recently been updated to make use spatially highly resolved USGS 0.5km MODIS based Land Cover Type 2 data (`https://archive.usgs.gov/archive/sites/landcover.usgs.gov/global_climatology.html`)

The parameters retrieved by CC4CL are constrained to the following ranges:

- The $\log_{10}$ of cloud optical depth at 0.55 μm: [-3 – 2.408]
- The effective radius (in μm): [0.1 – 35 (liquid) or 100 (ice)]
- The cloud top pressure (in hPa): [10 – 1200]
- Surface temperature (in K): [250 – 320]

In addition to the retrieved state parameters, a number of cloud variables are derived and stored in the global-level cloud products. Cloud top pressure is converted to cloud top height and temperature using the ECMWF temperature/pressure profiles. Cloud water path CWP is derived using the method of Han et al. [14]

$$CWP = \frac{4}{3}\frac{\tau \cdot r_{\text{eff}} \cdot \rho}{Q_{ext}}, \tag{42}$$

where Q_{ext}, the extinction coefficient, is assumed to be 2 for water and 2.1 for ice for wavelengths much less than r_{eff}. The density ρ is $1\,\text{g}\,\text{m}^{-3}$ for water and $0.9167\,\text{g}\,\text{m}^{-3}$ for ice. Depending on phase, CWP is also known as liquid water path (LWP) or ice water path (IWP).

More technical descriptions of CC4CL's inputs, outputs, and data formats, in addition to example data files, can be found at the project's code repository at `https://github.com/ORAC-CC/orac`.

Appendices

A Spectral band adjustment (SBA)

To mimic NOAA-19 AVHRR, for which the cloud detection and cloud phase determination were developed and fine-tuned spectral band adjustment factors (SBA) were determined. The SBAs (slope and offset) were inferred from linearly fitting synthetic measurements between pairs of sensors (sensor X and NOAA19 AVHRR). The synthetic measurements were calculated from a set of SCIAMACHY and IASI orbits. SCIAMACHY and IASI provide hyperspectral measurements throughout the visible (SCIAMACHY) and infrared (IASI) part of the electromagnetic spectrum. Convolving the spectral response functions (SRF) of AVHRR channels $0.6\mu m$, $0.9\mu m$, $10.8\mu m$ and $12.0\mu m$ over the SCIAMACHY and IASI spectra, synthetic AVHRR measurements in each SCIAMACHY and IASI footprint are inferred building a set of points which is the basis for the linear fitting. This SBAs are applied prior to cloud detection and cloud typing procedures. Near-infrared channels at $1.6\mu m$ and $3.7\mu m$ are not adjusted as the SCIAMACHY and IASI spectra do not cover the full AVHRR SRF of these channels. All inferred SBAs are given in Tables 5 and 6. In contrast to cloud detection and phase determination, the OE retrieval uses the individual SRFs thus SBAs are not required for the OE retrieval.

Table 5: Linear regression coefficients (slope and offset) applied as spectral band adjustment to either measured reflectances (R) or brightness temperature of all AVHRR-heritage channels (Ch) and sensors (used so far) to mimic NOAA-19 AVHRR. The subscript in the table's headline corresponds to the approximate central wavelengths of the channels: 0.6µm, 0.9µm, 1.6µm, 3.7µm, 10.8µm, 12.0µm. Reflectances in channels 0.6µm, 0.9µm and 1.6µm are generally not used in twilight and night conditions. Table (except SLSTR and SEVIRI coefficients) adopted from Stengel et al. [39]

	$R_{0.6}$ slope / offset	$R_{0.9}$ slope / offset	$R_{1.6}$ slope / offset	$BT_{3.7}$ slope / offset	$BT_{10.8}$ slope / offset	$BT_{12.0}$ slope / offset
			day			
noaa-5	1.009 / -0.174	1.011 / -0.102	1.000 / 0.000	0.985 / 3.681	0.999 / 0.236	1.000 / 0.000
noaa-6	1.012 / -0.027	1.003 / -0.052	1.000 / 0.000	0.976 / 6.078	0.999 / 0.300	1.000 / 0.000
noaa-7	1.009 / -0.036	1.007 / -0.007	1.000 / 0.000	1.010 / -2.531	1.000 / -0.198	0.991 / 1.991
noaa-8	1.010 / -0.009	1.003 / -0.048	1.000 / 0.000	0.985 / 3.277	0.999 / 0.201	1.000 / 0.000
noaa-9	1.009 / -0.013	1.006 / 0.011	1.000 / 0.000	1.014 / -3.535	1.000 / -0.215	0.988 / 2.770
noaa-10	1.010 / -0.044	1.005 / -0.020	1.000 / 0.000	1.001 / -0.462	0.999 / 0.469	1.000 / 0.000
noaa-11	1.009 / -0.010	1.005 / -0.012	1.000 / 0.000	1.008 / -2.286	1.000 / -0.170	0.989 / 2.443
noaa-12	1.008 / 0.012	1.005 / -0.029	1.000 / 0.000	0.986 / 3.190	1.001 / -0.212	0.994 / 1.383
noaa-13	1.000 / 0.000	1.000 / 0.000	1.000 / 0.000	1.000 / 0.000	1.000 / 0.000	1.000 / 0.000
noaa-14	1.008 / 0.016	1.011 / -0.026	1.000 / 0.000	0.992 / 2.122	1.001 / -0.446	0.995 / 1.081
noaa-15	1.005 / -0.027	1.006 / 0.047	1.000 / 0.000	1.012 / -3.984	1.000 / -0.136	0.990 / 2.145
noaa-16	1.006 / -0.039	1.009 / 0.057	1.000 / 0.000	1.015 / -4.572	1.000 / -0.095	0.997 / 0.561
noaa-17	1.004 / -0.021	1.008 / 0.053	1.000 / 0.000	0.998 / 0.037	1.000 / -0.185	0.990 / 2.112
noaa-18	1.002 / -0.013	1.015 / 0.066	1.000 / 0.000	0.994 / 1.422	1.000 / -0.214	0.997 / 0.626
noaa-19	1.000 / 0.000	1.000 / -0.000	1.000 / 0.000	1.000 / 0.000	1.000 / -0.000	1.000 / 0.000
noaa-20	1.000 / 0.000	1.000 / 0.000	1.000 / 0.000	1.000 / 0.000	1.000 / 0.000	1.000 / 0.000
metop-1	1.006 / -0.033	1.011 / 0.033	1.000 / 0.000	0.998 / 0.899	1.000 / -0.165	0.990 / 2.300
metop-2	1.006 / -0.033	1.006 / 0.038	1.000 / 0.000	1.013 / -3.203	1.000 / -0.196	0.991 / 1.981
modis-t	0.978 / 0.202	0.897 / -0.004	1.000 / 0.000	0.975 / 5.113	0.998 / 0.571	0.985 / 3.596
modis-a	0.979 / 0.201	0.897 / -0.005	1.000 / 0.000	0.976 / 4.413	0.998 / 0.674	0.985 / 3.614
atsr2	0.959 / 0.259	0.894 / -0.012	1.000 / 0.000	1.045 / -9.727	0.999 / 0.435	1.000 / 0.034
aatsr	0.956 / 0.259	0.893 / -0.013	1.000 / 0.000	1.005 / -1.764	0.999 / 0.268	1.003 / -0.753
msg1	0.997 / 0.009	0.945 / -0.148	1.000 / 0.000	1.015 / 0.864	1.001 / -0.149	0.992 / 1.985
msg2	0.997 / 0.010	0.949 / -0.163	1.000 / 0.000	1.008 / 2.875	1.001 / -0.271	0.994 / 1.311
msg3	1.000 / -0.015	0.945 / -0.167	1.000 / 0.000	1.010 / 2.367	1.001 / -0.166	0.993 / 1.760
msg4	0.997 / 0.004	0.946 / -0.164	1.000 / 0.000	1.004 / 3.512	1.001 / -0.283	0.992 / 1.914
s3a_slstr	0.956 / 0.258	0.896 / -0.009	1.000 / 0.000	1.011 / -2.299	0.999 / 0.219	0.998 / 0.611
s3b_slstr	0.955 / 0.258	0.896 / -0.009	1.000 / 0.000	1.010 / -1.976	1.000 / 0.109	0.998 / 0.464

Table 6: As table 5 but for twilight and night conditions.

	$R_{0.6}$ slope / offset	$R_{0.9}$ slope / offset	$R_{1.6}$ slope / offset	$BT_{3.7}$ slope / offset	$BT_{10.8}$ slope / offset	$BT_{12.0}$ slope / offset
twilight & night						
noaa-5	1.000 / 0.000	1.000 / 0.000	1.000 / 0.000	0.991 / 1.398	0.999 / 0.345	1.000 / 0.000
noaa-6	1.000 / 0.000	1.000 / 0.000	1.000 / 0.000	0.985 / 2.452	0.999 / 0.394	1.000 / 0.000
noaa-7	1.000 / 0.000	1.000 / 0.000	1.000 / 0.000	1.008 / -1.902	1.000 / -0.194	0.992 / 1.786
noaa-8	1.000 / 0.000	1.000 / 0.000	1.000 / 0.000	0.989 / 1.610	0.999 / 0.292	1.000 / 0.000
noaa-9	1.000 / 0.000	1.000 / 0.000	1.000 / 0.000	1.011 / -2.387	1.000 / -0.243	0.989 / 2.500
noaa-10	1.000 / 0.000	1.000 / 0.000	1.000 / 0.000	1.000 / -0.424	0.998 / 0.565	1.000 / 0.000
noaa-11	1.000 / 0.000	1.000 / 0.000	1.000 / 0.000	1.006 / -1.500	1.000 / -0.178	0.990 / 2.184
noaa-12	1.000 / 0.000	1.000 / 0.000	1.000 / 0.000	0.991 / 1.194	1.000 / -0.111	0.994 / 1.218
noaa-13	1.000 / 0.000	1.000 / 0.000	1.000 / 0.000	1.000 / 0.000	1.000 / 0.000	1.000 / 0.000
noaa-14	1.000 / 0.000	1.000 / 0.000	1.000 / 0.000	0.996 / 0.290	1.001 / -0.427	0.996 / 0.945
noaa-15	1.000 / 0.000	1.000 / 0.000	1.000 / 0.000	1.006 / -1.306	1.000 / -0.109	0.991 / 1.903
noaa-16	1.000 / 0.000	1.000 / 0.000	1.000 / 0.000	1.008 / -1.578	1.000 / 0.022	0.997 / 0.511
noaa-17	1.000 / 0.000	1.000 / 0.000	1.000 / 0.000	0.999 / -0.071	1.000 / -0.173	0.992 / 1.877
noaa-18	1.000 / 0.000	1.000 / 0.000	1.000 / 0.000	0.996 / 0.366	1.000 / -0.209	0.997 / 0.542
noaa-19	1.000 / 0.000	1.000 / 0.000	1.000 / 0.000	1.000 / 0.000	1.000 / 0.000	1.000 / 0.000
noaa-20	1.000 / 0.000	1.000 / 0.000	1.000 / 0.000	1.000 / 0.000	1.000 / 0.000	1.000 / 0.000
metop-1	1.000 / 0.000	1.000 / 0.000	1.000 / 0.000	1.000 / -0.040	1.001 / -0.218	0.991 / 2.053
metop-2	1.000 / 0.000	1.000 / 0.000	1.000 / 0.000	1.011 / -2.633	1.000 / -0.170	0.992 / 1.744
modis-t	1.000 / 0.000	1.000 / 0.000	1.000 / 0.000	0.979 / 4.234	0.997 / 0.782	0.987 / 2.963
modis-a	1.000 / 0.000	1.000 / 0.000	1.000 / 0.000	0.979 / 4.277	0.997 / 0.876	0.987 / 2.978
atsr	1.000 / 0.000	1.000 / 0.000	1.000 / 0.000	1.038 / -7.470	0.999 / 0.521	1.000 / 0.018
aatsr	1.000 / 0.000	1.000 / 0.000	1.000 / 0.000	1.002 / -0.548	0.999 / 0.265	1.003 / -0.667
msg1	1.000 / 0.000	1.000 / 0.000	1.000 / 0.000	1.036 / -9.296	1.001 / -0.138	0.992 / 1.783
msg2	1.000 / 0.000	1.000 / 0.000	1.000 / 0.000	1.032 / -7.445	1.001 / -0.238	0.995 / 1.178
msg3	1.000 / 0.000	1.000 / 0.000	1.000 / 0.000	1.034 / -7.719	1.001 / -0.133	0.993 / 1.585
msg4	1.000 / 0.000	1.000 / 0.000	1.000 / 0.000	1.028 / -6.587	1.001 / -0.231	0.993 / 1.722
s3a_slstr	1.000 / 0.000	1.000 / 0.000	1.000 / 1.000	1.010 / -2.286	0.9999 / 0.224	0.998 / 0.541
s3b_slstr	1.000 / 0.000	1.000 / 0.000	1.000 / 1.000	1.009 / -1.855	1.000 / 0.085	0.998 / 0.403

B Bayesian scene identification

Although not part of the operational CC4CL scheme used to produce the Phase I Cloud_cci products, the use of Bayesian statistics on the retrieval output to refine the cloud masking and phase selection – together described as scene identification – has been investigated and implemented as an option in the retrieval algorithm. A brief description of the methodology and initial results is provided here.

A posteriori Bayesian scene identification is concerned with answering the question, "What is the probability that a given retrieval result is consistent with the measurements and our prior knowledge of the atmospheric state?" Given an answer to that question for a range of assumed cloud and/or aerosol properties, we can further ask whether the measurements provide a clear indication of which set of those assumptions best describes the observations.

As described in section 2, an OEM retrieval is constructed based on maximising the Bayesian probability of the retrieved state, conditional on the measurements and *a priori* constraints. This formulation assumes that the uncertainties in both the measurement and *a priori* are Gaussian and that the retrieval is nearly linear within

the region defined by these uncertainties. Rodgers [31] shows that the cost function $J(\vec{x})$ is directly related to this conditional probability through the expression

$$P(\vec{x}|\vec{y},\ \vec{x_{\rm a}}) = P(\vec{x_{\rm a}}) \exp\left(-\frac{J(\vec{x})}{2}\right). \tag{43}$$

It is clear, therefore, that a well-characterised optimal estimation retrieval scheme not only provides state estimates with fully propagated uncertainties but can also provide probabilistic measures of the consistency of the state with the measurement and *a priori*.

If we examine the expression for the OEM cost function:

$$J(\vec{x}) = [\vec{y}(\vec{x}) - \vec{y_{\rm m}}]\,\mathbf{S_y}^{-1}\,[\vec{y}(\vec{x}) - \vec{y_{\rm m}}]^T + (\vec{x} - \vec{x_{\rm a}})\,\mathbf{S_a}^{-1}\,(\vec{x} - \vec{x_{\rm a}})^T, \tag{44}$$

we can identify the two terms on the right hand side: the measurement cost $J_{\rm m}$ and the *a priori* cost $J_{\rm a}$. In situations where the forward model is a good representation of the true atmosphere, in that it is able to reproduce the observed TOA radiances while remaining consistent with the prior constraints, these terms should represent random samples from normal distributions with differing degrees of freedom. $J_{\rm a}$ is the degrees of freedom equal the number of elements in the state vector. $J_{\rm m}$ is equal to the degrees for freedom of signal $d_{\rm s}$, which is the number of independent pieces of information provided by the measurement above the level of noise and is defined by:

$$d_{\rm s} = {\rm tr}\left(\mathbf{K}\mathbf{S_a}\mathbf{K}^T\left[\mathbf{K}\mathbf{S_a}\mathbf{K}^T + \mathbf{S_y}\right]^{-1}\right), \tag{45}$$

where ${\rm tr}\,(\mathbf{A})$ denotes the trace of the matrix $\mathbf{A}$.

Thus, by comparing the cost function components to the χ^2 distribution — the distribution of the sum of the squares of a set of normally distributed random variables — with the appropriate degrees of freedom, we can calculate the probability that any given retrieval lies within the expected range described by the measurement and *a priori* uncertainties. This is the standard χ^2 test and provides the probabilistic measure of consistency for each retrieval. The test can be performed separately for both the measurement and *a priori* constraint and the resulting probabilities multiplied to produce an overall value, denoted by $\mathcal{P}$.

In the case where the cloud phase is ambiguous (see section 2.2 and section D.2), the $\mathcal{P}$ statistic can provide useful additional insight. Selecting the phase with the highest $\mathcal{P}$ value is equivalent to selecting that with the lowest cost, but in addition one can ascertain the following:

- The probability that each phase is the correct one, based on the measurement and *a priori* constraints. If no phase provides a result which is consistent with the measurement then the atmospheric state lies outside the range of assumptions made in the forward model and the results should be treated with caution.

- Under the assumption that only one phase can be the correct one, we assume that the one with the highest probability is the correct one. In general terms, if N phases have been tried in the retrieval, then the probability that the nth phase is the correct one can be written:

$$\mathcal{P}'_{\rm n} = \frac{\mathcal{P}_{\rm n}}{\sum_{i=1}^{N}\mathcal{P}_i}. \tag{46}$$

The question of phase discrimination can also be generalised to include cloud detection, through the inclusion of background aerosol types (such as maritime aerosol over the oceans) and episodic aerosols, such as desert dust, which might be detected as cloud by traditional threshold-based cloud flagging.

As the $\mathcal{P}$ statistic represents the Bayesian probability of a particular state being consistent with the measurements and prior constraints, within the framework of the retrieval forward model and uncertainty budget, it offers two key advantages:

1. The probability $\mathcal{P}$ represents the true constraint on the atmospheric state provided by the measurement, under the assumptions made in the retrieval. Cloud retrievals are generally under-constrained and a probability provides a intuitive and easily understood measure of the ambiguity of a retrieval result.

2. The availability of a probabilistic cloud mask and phase selection provides a quantitative method of combining the constraint provided by the retrieval itself with prior and posterior constraints through Bayesian methods.

The accuracy — in terms of the probability values produced — of this approach does require that the retrieval uncertainty budget be well understood. If measurement and forward modelling uncertainties are inaccurate, the resulting PDF of the retrieval cost function will not follow the χ^2 distribution and the values of $\mathcal{P}$ produced will be erroneous.

C Look-up tables

The reflection/transmission/emissivity operators are calculate off-line. They can be produced at a specific wavelength λ or for a waveband. In the latter case the operator X_c for channel c is calculated from

$$X_c = \frac{\int_{\tilde{\nu}_1}^{\tilde{\nu}_2} X(\tilde{\nu})\phi(\tilde{\nu})\, d\tilde{\nu}}{\int_{\tilde{\nu}_1}^{\tilde{\nu}_2} \phi(\tilde{\nu})\, d\tilde{\nu}}$$

where ϕ is the spectral response of the channel with limits $[\tilde{\nu}_1, \tilde{\nu}_2]$. Typically 20 - 30 integration points captures the spectral variation of ϕ.

D SEVIRI_ML

With Cloud_cci version 3 the cloud detection and phase determination ANNs are now integrated into a software suite named SEVIRI_ML (`https://github.com/danielphilipp/seviri_ml`). SEVIRI_ML is a Python-based machine learning software suite to predict various cloud properties from SEVIRI measurements including the cloud mask and cloud phase used for version 3. It is also possible to run the version 1 and version 2 CMA and CPH ANNs within SEVIRI_ML. SEVIRI_ML has Fortran and C interfaces so that it can be easily integrated into and used with CC4CL. The latest version of SEVIRI_ML can also predict a CTP, CTT, Multilayer Flag (MLAY) and Cloud Base Height (CBH) besides the already known CMA and CPH explained below. For version 3 the CMA and CPH ANNs have been completely re-trained with a larger training dataset to improve the CMA and CPH performance. Especially the detection of thin clouds and the distinction of clouds from aerosols was focused. In contrast to the heritage channel ANNs in section 2.1 and section 2.2, SEVIRI_ML takes advantage of the full spectral capabilities of SEVIRI. As CTP, CTT, MLAY and CBH are no official products they are not further described below.

D.1 Cloud detection

For version 3, a completely new CMA ANN has been trained. At this stage there is only one cloud mask network for all illumination-surface type scenarios. The training data are based on collocations between SEVIRI L1B, ERA5, land-sea masking and CALIPSO Cloud Optical Depth (COD) data. In contrast to the 4 months in version 2, now all 12 months of 2018 were collocated yielding $\approx$ 10.0E6 collocations ($\approx$ 2.4E6 collocations in version 2) for training. As a result, a pseudo CALIPSO optical depth (ANNCOD) regression value is computed (mimicked) and converted into a binary cloud mask by applying a threshold.

The ANN is a feed-forward multilayer perceptron consisting of a input layer with 16 input features, 3 hidden layers with 125 neurons each and a single neuron output layer outputting the target ANNCOD regression value ranging between 0 and 1. Input to the cloud masking network is listed in table 8. Prior to training COD's greater than 1 have been set to 1 and input data are standardized using z-score scaling before training to limit the data range. For training SEVIRI L1B infrared channels were calibrated using the Global Space-based Inter-Calibration System (GSICS) calibration coefficients and visible channels using the standard IMPF coefficients [9]. Because at this point visible channels in CC4CL are calibrated using the NASA coefficients [8], a linear correction is applied to convert from NASA to the expected IMPF calibration only for the SEVIRI ANN. With this correction the CC4CL data and SEVIRI ANN expectations are harmonized. The linear correction coefficients are listed in table 7.

Table 7: NASA to IMPF visible channel calibration correction parameters for each Meteosat Second Generation (MSG).

	VIS 0.6µm		**VIS 0.8µm**		**VIS 1.6µm**	
	Slope	**Offset**	**Slope**	**Offset**	**Slope**	**Offset**
MSG1	0.85628	0.00000	0.91591	0.00000	1.05427	0.00000
MSG2	0.91689	0.00000	0.93875	0.00000	1.04209	0.00000
MSG3	0.89353	0.00000	0.95154	0.00000	1.03764	0.00000
MSG4	0.90091	0.00000	0.97954	0.00000	1.06372	0.00000

Table 8: Input features to the cloud masking and cloud phase determination neural networks. For both networks the input is identical. IMPF calibration = EUMETSAT Image Processing Facility calibration coefficients ([9]). GSICS calibration = Global Space-based Inter-Calibration System calibration coefficients.

	Input feature	**Remark**
01	SEVIRI L1B VIS 0.6µm	IMPF calibrated
02	SEVIRI L1B VIS 0.8µm	IMPF calibrated
03	SEVIRI L1B NIR 1.6µm	IMPF calibrated
04	SEVIRI L1B IR 3.9µm	GSICS calibrated
05	SEVIRI L1B IR 6.2µm	GSICS calibrated
06	SEVIRI L1B IR 7.3µm	GSICS calibrated
07	SEVIRI L1B IR 8.7µm	GSICS calibrated
08	SEVIRI L1B IR 10.8µm	GSICS calibrated
09	SEVIRI L1B IR 12.0µm	GSICS calibrated
10	SEVIRI L1B IR 13.4µm	GSICS calibrated
11	SEVIRI L1B IR (8.7µm – IR 10.8µm)	GSICS calibrated
12	SEVIRI L1B IR (12.0µm – IR 10.8µm)	GSICS calibrated
13	Satellite Zenith Angle	
14	Solar Zenith Angle	
15	ERA5 skin temperature	
16	Land-sea mask	

Cloud detection thresholds:

For version 3 one threshold of 0.13 is applied to the ANNCOD outputted by the cloud detection ANN to determine the binary cloud mask. Analysis revealed that the threshold variation for all the different surface type-illumination scenarios is rather small (≈ 0.03) allowing us to initially avoid the increasing complexity.

Thresholds are based on an optimization of validation scores. To calculate the scores a CALIPSO cloud mask derived by thresholding its COD at 0.0 is collocated with the ANNCOD for May 2017. It is important to mention that May 2017 has not been used for training so that the here used data have never been seen by the network. For each threshold the 'accumulated score error' (ASE) is calculated. It is a measure of how much a set of chosen scores is distanced from its perfect value. For each of the chosen scores at each threshold, the differences between the score value and the score's best possible value is calculated. For each threshold all the differences are summed up yielding the ASE. Now, the threshold minimizing the ASE can be determined.

Cloud detection uncertainty:
To calculate the scores, a CALIPSO cloud mask derived by thresholding its COD at 0.0 is collocated with the binary cloud mask for May 2017 (independent from training data). The scores show a clear dependence on the distance between the ANNCOD and the respective threshold allowing an approximation of the cloud detection uncertainty on a pixel basis. By binning the differences between the threshold and the regression value and calculating the uncertainty based on CALIPSO scores for each bin a curve is determined (blue curves in figure 3). Linear regression parameters allow us calculate the probability of incorrect cloud mask as a function of normalized ANNCOD-threshold distance (red lines in figure 3). Regression parameters can be obtained from figure 3.

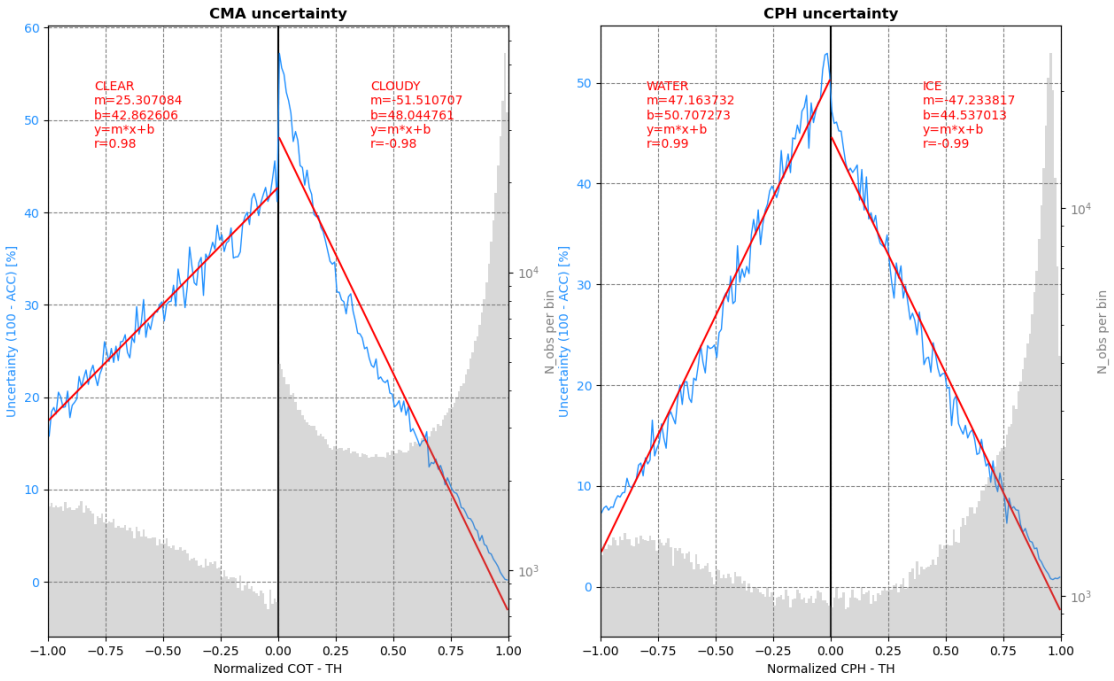

Figure 3: External SEVIRI neural network cloud mask (CMA) and cloud phase (CPH) uncertainty including regression parameters.

D.2 Cloud type and phase determination

Cloud type:
As for the AVHRR-heritage part in section 2.2.

Cloud phase:
For version 3, a completely new CPH ANN has been trained. At this stage there is only one cloud phase network for all illumination-surface type scenarios. The training data are based on collocations between SEVIRI L1B, ERA5, land-sea masking and CALIPSO Cloud Optical Depth (COD) data. In contrast to the 4 months in version 2, now all 12 months of 2018 were collocated yielding $\approx$ 10.0E6 collocations ($\approx$ 2.4E6 collocations in version 2) for training. However, only $\approx$ 7.0E6 collocations are used for CPH ANN training as clear pixels ($\approx$ 30%) are not relevant. As a result, a CPH regression value between 0 and 1 is predicted and subsequently converted into a binary CPH by applying a threshold.

The ANN is a feed-forward multilayer perceptron consisting of a input layer with 16 input features, 2 hidden layers with 150 neurons each and a single neuron output layer outputting the target CPH regression value ranging between 0 and 1. Input to the CPH network is listed in table 8. For training SEVIRI L1B infrared channels were calibrated using the Global Space-based Inter-Calibration System (GSICS) calibration coefficients and visible channels using the standard IMPF coefficients [9]. Because at this point visible channels in CC4CL are calibrated using the NASA coefficients [8], a linear correction is applied to convert from NASA to the expected IMPF calibration only for the SEVIRI ANN. With this correction the CC4CL data and SEVIRI ANN expectations are harmonized. The linear correction coefficients are listed in table 7. Input data are standardized using z-score scaling before training to limit the data range.

Cloud phase thresholds:
At this stage one threshold of 0.50 is applied to the outputted by the cloud phase ANN to determine the binary CPH. Analysis revealed that the threshold variation for all the different surface type-illumination scenarios is rather small ($\approx$ 0.02) allowing us to initially avoid the increasing complexity. Thresholds are based on an optimization of validation scores. To calculate the CALIPSO CPH is collocated with the cloud phase regression value for May 2017. It is important to mention that May 2017 has not been used for training so that the here used data have never been seen by the network. For each threshold the 'accumulated score error' (ASE) is calculated. It is a measure of how much a set of chosen scores is distanced from its perfect value. For each of the chosen scores at each threshold, the differences between the score value and the score's best possible value is calculated. For each threshold all the differences are summed up yielding the ASE. Now the threshold minimizing the ASE can be determined.

Cloud phase uncertainty:
To calculate the scores, the CALIPSO cloud phase is collocated with the binary CPH for May 2017 (independent from training data). The scores show a clear dependence on the distance between the ANN regression output and the respective threshold allowing an approximation of the cloud phase uncertainty on a pixel basis. By binning the differences between the threshold and the regression value and calculating the uncertainty based on CALIPSO scores for each bin a curve is determined (blue curves in figure 3). Linear regression parameters allow us calculate the probability of incorrect cloud phase as a function of normalized ANN regression output-threshold distance (red lines in figure 3). Regression parameters can be obtained from figure 3.

Improvements from version 2 to version3:

- Trained new version 3 ANN networks with about 4 times more training data.

- Updated thresholds and uncertainty characterization focusing on thin clouds and distinction from aerosol.
- Implemented a handling of invalid 3.9 μm measurements for very cold clouds. In case an invalid 3.9 μm pixel is detected, this pixels is automatically set to cloudy and ice phase.
- Improved Python-C-Fortran interface for better data propagation through the programming languages for use of SEVIRI_ML with CC4CL.
- Added an internal spectral band adjustment to process Goes-16 ABI, Goes-17 ABI and Himawari AHI with the SEVIRI ANNs.

References

[1] ACRI-ST IPF Team, Product Data Format Specification - SLSTR Level 1 Products, S3IPF.PDS.005.1, Sentinel Online, Issue 2.9, 2019.
URL: (last accessed 4-Mar-2021) https://sentinels.copernicus.eu/documents/247904/1872792/Sentinel-3-SLSTR-Product-Data-Format-Specification-Level-1.pdf/26cb7851-22fa-44c1-b22b-428a8eb5e6c3?t=1611043060001.

[2] Baran, A. J. and Havemann, S., The dependence of retrieved cirrus ice-crystal effective dimension on assumed ice-crystal geometry and size-distribution function at solar wavelengths, Q. J. R. Meteorol. Soc., 130, 2153–2167, doi: 10.1256/qj.03.154, 2004.

[3] Baran A. J., Shcherbakov V. N., Baker B. A., Gayet J. F. and Lawson RP., On the scattering phase function of non-symmetric ice crystals, Q. J. R. Meteor Soc., 131, 260916, 2005.

[4] Birks, A., Improvements to the AATSR IPF relating to land surface temperature, ESA Technical note. AATSR Product Handbook, Issue 1.2, European Space Agency, 2004.

[Cox et al]

[6] Cox, C. and Munk, W., Measurement of the roughness of the sea surface from photograhs on the Sun's glitter, J. Opt. Soc. Am., 44, 838–850, doi:10.1364/JOSA.44.000838, 1954.

[7] Cox, C. and Munk, W., Statistics of the sea surface derived from Sun glitter, J. Mar. Res., 13, 198–227, 1954.

[8] Doelling, D., Haney, C., Bhatt, R., Scarino, B., & Gopalan, A. (2018). Geostationary visible imager calibration for the CERES SYN1deg edition 4 product. Remote Sensing, 10(2), 288.

[9] EUMETSAT, Radiometric Calibration of MSG SEVIRI Level 1.5 Image Data in Equivalent Spectral Blackbody Radiance, Doc. No. EUM/OPS-MSG/TEN/03/0064, `https://www-cdn.eumetsat.int/files/2020-04/pdf_ten_msg_seviri_rad_calib.pdf`, Last access 16/03/2021.

[10] EUMETSAT, MSG Level 1.5 Image Data Format Description, Doc. No. EUM/MSG/ICD/105, `https://www-cdn.eumetsat.int/files/2020-05/pdf_ten_05105_msg_img_data.pdf`, Last access 16/03/2021.

[11] Etxaluze, M. and Smith D., Sentinel-3 SLSTR Uncertainties in Level-1 Products Algorithm and Theoretical Basis Document, Issue 3, EUMETSAT Technical Note, Doc. No. SLSTR-RAL-EUM-TN-003, `https://www-cdn.eumetsat.int/files/2020-04/pdf_ss_s3_slstr_l1_atbd.pdf`, Last access 08/03/2021.

[12] Grosvenor, D. P., Sourdeval, O., Zuidema, P., Ackerman, A., Alexandrov, M. D., Bennartz, R., Boers, R., Cairns, B., Chiu, J. C., Christensen, M., Deneke, H., Diamond, M., Feingold, G., Fridlind, A., Hünerbein, A., Knist, C., Kollias, P., Marshak, A., McCoy, D., Merk, D., Painemal, D., Rausch, J., Rosenfeld, D., Russchenberg, H., Seifert, P., Sinclair, K., Stier, P., van Diedenhoven, B., Wendisch, M., Werner, F. Wood, R., Zhang, Z. and Quaas, J., Remote Sensing of Droplet Number Concentration in Warm Clouds: A Review of the Current State of Knowledge and Perspectives, Rev. Geophys., 56, 2, 409–453, doi:10.1029/2017RG000593, 2018.

[13] Gryspeerdt, E., Quaas, J. and Bellouin, N., Constraining the aerosol influence on cloud fraction, J. Geophys. Res. Atmos., 121, 3566–3583, doi:10.1002/2015JD023744, 2016.

[14] Han, Q., Rossow, W. B. and Lasis, A. A., Near-Global Survey of Effective Droplet Radii in Liquid Water Clouds Using ISCCP Data, J. of Climate, 7, 465–497, 1994.

[15] Hersbach, H., Bell, B., Berrisford, P., Biavati, G., Horányi, A., Muñoz Sabater, J., Nicolas, J., Peubey, C., Radu, R., Rozum, I., Schepers, D., Simmons, A., Soci, C., Dee, D., Thépaut, J-N. (2018): ERA5 hourly data on single levels from 1979 to present. Copernicus Climate Change Service (C3S) Climate Data Store (CDS), 2018. (Accessed on 05-Mar-2021), DOI: 10.24381/cds.adbb2d47

[16] Koepke, P., Effective Reflectance of Oceanic Whitecaps, AO, 23, 1816–1824, doi:10.1364/AO.23.001816, 1984.

[17] Lean, K., Empirical methods for detecting atmospheric aerosol events from satellite measurements, MPhys. Project Report, University of Oxford, `http://www.atm.ox.ac.uk/group/eodg/mphys_reports/2009_Lean.pdf`, 2009.

[18] Levenberg, K., A method for the solution of certain nonlinear problems in least squares, Quart. Appl. Math., 2, 164–168, 1944.

[19] Lucht, W., Schaaf, C.B., and Strahler, A.H., An Algorithm for the Retrieval of Albedo from Space Using Semiempirical BRDF Models, Atmospheric Science, Surface Radiative Properties/BRDFs, TGRS, 38, 977–998, doi:10.1109/36.841980, 2000.

[20] Nolin, A., Armstrong, R. L. and Maslanik, J., Near-Real-Time SSM/I-SSMIS EASE-Grid Daily Global Ice Concentration and Snow Extent. Boulder, Colorado USA: National Snow and Ice Data Center, 1998.

[21] Marquardt, D. W., An algorithm for least-squares estimation of nonlinear parameters, SIAM, J. Appl. Math., 11, 431–441, doi:10.2307/2098941, 1963.

[22] McGarragh, G. R., Poulsen, C. A., Thomas, G. E., Povey, A. C., Sus, O., Stapelberg, S., Schlundt, C., Proud, S., Christensen, M. W., Stengel, M., Hollmann, R., and Grainger, R. G.: The Community Cloud retrieval for CLimate (CC4CL) ? Part 2: The optimal estimation approach, Atmos. Meas. Tech., 11, 3397-3431, https://doi.org/10.5194/amt-11-3397-2018, 2018.

[23] Meerkötter, R. and Zinner, T., Satellite remote sensing of cloud base height for convective cloud fields: A case study, Geophys. Res. Lett., 34, 17, 2–5, doi:10.1029/2007GL030347, 2007.

[24] Morel, A. and Prieur, L., Analysis of Variations in Ocean Color, Limnology and Oceanography, 22, 709–722, doi:10.4319/lo.1977.22.4.0709, 1977.

[25] MTG Level 2 Processing Specification Document, Document Number EUM/MTG/SPE/12/ 1078, March 2014.

[26] Pavolonis, M. J. and Heidinger A. K., Daytime Cloud Overlap Detection from AVHRR and VIIRS, J. Appl. Meteor., 43, 762–778, doi:10.1175/2099.1, 2004.

[27] Pavolonis, M. J., Heidinger A. K., and Uttal, T., Daytime Global Cloud Typing from AVHRR and VIIRS: Algorithm Description, Validation, and Comparisons, J. Appl. Meteor., 44, 804-826, doi:10.1175/JAM2236.1, 2005.

[28] Poulsen, C. A., Siddans, R., Thomas, G. E., Sayer, A. M., Grainger, R. G., Campmany, E., Dean, S. M., Arnold, C., and Watts, P. D., Cloud retrievals from satellite data using optimal estimation: evaluation and application to ATSR, Atmos. Meas. Tech., 5, 1889–1910, doi:10.5194/amt-5-1889-2012, 2012.

[29] Prata, A. T., Povey, A., Grainger, R. G., and Proud, S., Uncertainties due to the use of assumed ice properties, Supplementary Material, Algorithm Theoretical Baseline Document v8.0 Community Cloud retrieval for Climate (CC4CL), 2022.

[PVIR] Product validation and inter comparison report, `http://www.esa-cloud-cci.org/sites/default/files/documents/public/Cloud_cci_D4.1_PVIR_v5.1.pdf`

[31] Rodgers, C. D., Inverse methods for atmospheric sounding: Theory and Practice. Series on Atmospheric, Oceanic and Planetary Physics, Vol. 2, World Scientific, 2000.

[32] Saunders, R. W., Matricardi, M. and Brunel, P., An Improved Fast Radiative Transfer Model for Assimilation of Satellite Radiance Observations, Q. J. R. Meteor. Soc., 125, 1407–1425, 1999.

[33] Sayer A. M, Poulsen, C. A., Arnold, C., Campmany, E., Dean, S., Ewen, G. B. L., Grainger, R. G., Lawrence, B. N., Siddans, R., Thomas, G. E., and Watts, P. D., Global retrieval of ATSR cloud parameters and evaluation (GRAPE): dataset assessment Atmos. Chem. Phys., 11, 3913–3936, doi:10.5194/acp-11-3913-2011, 2011.

[34] Sayer, A. M., Thomas, G. E. and Grainger, R. G., A sea surface reflectance model for (A)ATSR, and application to aerosol retrievals, Atmos. Meas. Tech., 2010, 3, 813–838, 4, 2010

[35] Schaaf, C. B., F. Gao, A. H. Strahler, W. Lucht, X. Li, T. Tsang, N. C. Strugnell, X. Zhang, Y. Jin, J.-P. Muller, P. Lewis, M. Barnsley, P. Hobson, M. Disney, G. Roberts, M. Dunderdale, C. Doll, R. d'Entremont, B. Hu, S. Liang, and J. L. Privette, and D. P. Roy., First Operational BRDF, Albedo and Nadir Reflectance Products from MODIS, Remote Sens. Environ., 83, 135–148, 2002.

[36] Schaepman-Strub, G., Schaepman, M. E., Painter, T. H., Dangel, S., Martonchik J. V., Reflectance quantities in optical remote sensing — definitions and case studies., Remote Sens. Environ., 103, 27–42, 2006.

[37] Seemann, S. W., Borbas, E. E., Knuteson, R. O., Stephenson, G. R. and Huang, H.-L. Development of a Global Infrared Land Surface Emissivity Database for Application to Clear Sky Sounding Retrievals from Multi-spectral Satellite Radiance Measurements., Appl. Meteor. Climatol., 47, 108–123, 2007.

[38] R. Siddans, C. Poulsen, E. Carboni Cloud Model for Operational Retrievals from MSG SEVIRI Final Report DRAFT Version 1.0, Eumetsat Contract EUM/CO/07/4600000463/PDW, January 26, 2011

[39] Stengel, M., Stapelberg, S., Sus, O., Schlundt, C., Poulsen, C., Thomas, G., Christensen, M., Carbajal Henken, C., Preusker, R., Fischer, J., Devasthale, A., Willén, U., Karlsson, K.-G., McGarragh, G. R., Proud, S., Povey, A. C., Grainger, R. G., Meirink, J. F., Feofilov, A., Bennartz, R., Bojanowski, J. S., and Hollmann, R.: Cloud property datasets retrieved from AVHRR, MODIS, AATSR and MERIS in the framework of the Cloud_cci project, Earth Syst. Sci. Data, 9, 881-904, https://doi.org/10.5194/essd-9-881-2017, 2017.

[40] Sus, O., Stengel, M., Stapelberg, S., McGarragh, G., Poulsen, C., Povey, A. C., Schlundt, C., Thomas, G., Christensen, M., Proud, S., Jerg, M., Grainger, R., and Hollmann, R.: The Community Cloud retrieval for CLimate (CC4CL) – Part 1: A framework applied to multiple satellite imaging sensors, Atmos. Meas. Tech., 11, 3373-3396, https://doi.org/10.5194/amt-11-3373-2018, 2018

[41] Stamnes K., Tsay S.C., Wiscombe W. and Jayaweera K., Numerically stable algorithm for discrete ordinate method radiative transfer in multiple scattering and emitting layered media., Appl. Opt., 12, 2502–2509, 1988.

[42] Takano, Y., and Liou, K. N., Solar radiative transfer in cirrus clouds. Part I: Single-scattering and optical properties of hexagonal ice crystals., J. Atmos. Sci., 46, 3–19, 1989.

[43] Thomas, G. E., Carboni, E., Sayer, A. M., Poulsen, C. A., Siddans, R. and Grainger, R. G., Oxford-RAL Aerosol and Cloud (ORAC): aerosol retrievals from satellite radiometers, in *Satellite aerosol remote sensing over land*, Kokhanovsky, A. A. and de Leeuw, G. (eds.), Springer-Praxis, 2009.

[44] Wanner, W., Strahler, A. H., Hu, B., Lewis, P., Muller, J.-P., Li, X., Barker Schaaf, C. L., and Barnsley, M. J., Global Retrieval of Bidirectional Reflectance and Albedo Over Land from EOS MODIS and MISR Data: Theory and Algorithm, JGR, 102, D14, 17143–17161, doi:10.1029/96JD03295, 1997.

[45] Watts, P. D., Mutlow, C. T., Baran, A. J. and Zavody, A. M., Study on cloud properties derived from Meteosat Second Generation Observations. Eumetsat Report, `http://www.eumetsat.int/Home/index.htm`, 1998

[46] Yang, P., L. Bi, B. A. Baum, K. Liou, G. W. Kattawar, M. I. Mishchenko, and B. Cole, 2013: Spectrally Consistent Scattering, Absorption, and Polarization Properties of Atmospheric Ice Crystals at Wavelengths from 0.2 to 100 ?m. J. Atmos. Sci., 70, 330?347, https://doi.org/10.1175/JAS-D-12-039.1

[47] Zhang Z., Yang, P., Kattawar, G., Riedi, J., Labonnote, L. C.-, Baum, B. A., Platnick, S., and Huang, H.-L., Influence of ice particle model on satellite ice cloud retrieval: lessons learned from MODIS and POLDER cloud product comparison, Atmos. Chem. Phys., 9, 7115–7129, 2009.